

ARTICLE

CNTD1 is crucial for crossover formation in female meiosis and for establishing the ovarian reserve

Anna J. Wood¹, Rania M. Ahmed¹, Leah E. Simon¹, Rachel A. Bradley¹, Stephen Gray², Ian D. Wolff¹, and Paula E. Cohen¹

In meiotic prophase I, hundreds of DNA double-strand breaks are formed and subsequently repaired as noncrossovers or crossovers (COs). COs are essential for accurate chromosome segregation during the first meiotic division, and errors in this process result in aneuploidy, birth defects, or infertility. Such errors are more pronounced in females compared with males, indicating that CO regulation and surveillance are sexually dimorphic. We demonstrate here dual roles of cyclin N-terminal domain containing 1 (CNTD1) in ensuring appropriate CO between homologous chromosomes in oocytes and in establishing the pool of follicles in the postnatal ovary. CNTD1-deficient oocytes fail to form COs and exhibit a severely depleted follicle pool shortly after birth, which is temporally distinct from previously reported CO mutants. Further investigation indicates that follicle loss is CHK2-dependent, resulting from inappropriate retention of HORMAD1 and the absence of SKP1. These findings indicate that CNTD1 plays novel roles in CO designation and establishment of the follicular reserve in female mammals.

Introduction

Meiosis is a specialized cellular division process that gives rise to genetically unique haploid gametes for sexual reproduction. Meiosis involves one round of DNA duplication and two reductive cell divisions. In meiosis I, homologous chromosomes must pair and segregate accurately, and in meiosis II, sister chromatids separate, reminiscent of mitosis. There is a distinct sexual dimorphism in the success of mammalian meiosis, as underscored by the fact that 10-70% of human oocytes exhibit aneuploidy compared with 3-5% of spermatocytes (Gruhn and Hoffmann, 2022; Gruhn et al., 2013; Hassold and Hunt, 2001; Hunt and Hassold, 2008; Morelli and Cohen, 2005; Nagaoka et al., 2012; Wang et al., 2017). Interestingly, a majority of the nondisjunction events that lead to an uploidy occur at the first meiotic division, arising from defects in crossover (CO) regulation, placement, and/or designation, which are exacerbated by weakened cohesion between homologous chromosomes and ineffective quality control checkpoints (Hassold and Hunt, 2001; Mihalas et al., 2024; Nagaoka et al., 2012). This raises the question of how CO regulation may differ between the sexes in mammals.

Homologous recombination is initiated by the formation of hundreds of DNA double-strand breaks (DSBs), each of which must be repaired prior to metaphase I entry. In mice, the majority of DSBs (~90%) are repaired as noncrossovers (NCOs), while the remaining DSBs are repaired as COs. These COs are crucial for ensuring homolog interactions until the first meiotic division. Thus, it is not surprising that the distribution and

frequency of COs across the genome must be tightly regulated to prevent improper chromosome segregation (Gray and Cohen, 2016; Hunter, 2015). The initiation of DSBs occurs in prophase of meiosis I and is catalyzed by the topoisomerase-like protein SPO11 and its partner proteins (Keeney et al., 1997; Romanienko and Camerini-Otero, 2000; Gray and Cohen, 2016; Tran and Schimenti, 2019). Subsequently, the RecA homologs RAD51 and DMC1 facilitate the induction of homology search for repair of these DSBs toward CO or NCO fates (Bishop et al., 1992; Cao et al., 1990; Cloud et al., 2012; Hinch et al., 2020; MacQueen, 2015; Yoshida et al., 1998). The former are further processed into COs by a highly regulated network of pro-CO proteins.

DSB repair intermediates destined to be repaired as COs are further processed by licensing (MutSy: MSH4 and MSH5) and designation (MutLy: MLH1 and MLH3) factors (de Vries et al., 1999; Edelmann et al., 1999; Gray and Cohen, 2016; Kneitz et al., 2000; Milano et al., 2019), which form large multiprotein complexes at the site of the DNA lesion. For example, licensing is dependent on the recruitment of two RING finger proteins, RNF212 and RNF212B (Condezo et al., 2024; Qiao et al., 2014, 2018; Reynolds et al., 2013). However, not all MutSy/RNF212/RNF212B-loaded sites are destined to become COs. Instead, ultimate CO designation requires the recruitment of a large group of regulators alongside MutLy, including HEI10, cyclin N-terminal domain containing 1 (CNTD1), PRR19, and CDK2 (Bondarieva et al., 2020; Gray et al., 2020; Holloway et al., 2014; Palmer et al., 2020; Qiao et al., 2014; Reynolds et al., 2013; Ward

¹Department of Biomedical Sciences and Cornell Reproductive Sciences Center (CoRe), Cornell University, Ithaca, NY, USA; ²School of Life Sciences, University of Nottingham, UK.

Correspondence to Paula E. Cohen: paula.cohen@cornell.edu; Ian D. Wolff: ian.wolff@cornell.edu.

© 2025 Wood et al. This article is distributed under the terms as described at https://rupress.org/pages/terms102024/.





et al., 2007). How these pro-CO factors orchestrate the designation of a subset of the \sim 150 MutS γ sites to become COs is a major question in the field.

Previous studies in our laboratory revealed a critical role of CNTD1 in the process of CO designation in male meiosis. CNTD1 is an ortholog of *Caenorhabditis elegans* crossover site-associated 1 (COSA-1) (Yokoo et al., 2012). *cosa-1* mutant worms exhibit a high rate of chromosome missegregation due to an absence of chiasmata (Yokoo et al., 2012). COSA-1 is a cyclin B-related protein, interacting in the nematode germline with the cyclin-dependent kinase, CDK2, to facilitate phosphorylation (and stabilization) of MSH-5 at nascent COs (Haversat et al., 2022; Zhang et al., 2021, *Preprint*).

In mouse spermatocytes, CNTD1 appears at pachynema of prophase I, where it colocalizes with MutLy and CO-associated CDK2 (Gray et al., 2020; Holloway et al., 2014). Loss of CNTD1 in males results in the complete absence of epididymal spermatozoa, leading to infertility (Gray et al., 2020; Holloway et al., 2014). Spermatocytes from Cntd1^{-/-} males show normal assembly of the synaptonemal complex (SC) and early DSB processing stages. By pachynema, Cntd1-/- spermatocytes show elevated and persistent MutSy foci through to late pachynema, and failure to accumulate CO-associated MutLy and CDK2, leading to severe meiotic progression defects at metaphase I (Gray et al., 2020; Holloway et al., 2014). Interestingly, and unlike the situation for worm COSA-1, the CNTD1 protein in the testis may lack a critical cyclin homology domain in its N terminus, possibly arising as a result of a predicted alternative translation start site within exon 3 (Gray et al., 2020). Accordingly, both yeast twohybrid analysis and immunoprecipitation from testis extracts reveal that CNTD1 does not bind CDK2 and thus does not act as a canonical cyclin during prophase I in the mouse, suggesting a different mechanism of action to that of COSA-1 (Gray et al., 2020; Haversat et al., 2022; Yokoo et al., 2012).

Given the sexual dimorphism in prophase I regulation observed in mammals, we were interested in investigating the role of CNTD1 in female meiosis. The timing and duration of meiosis differ between the sexes, occurring as continuous waves of meiotic initiation throughout postnatal life in males, and occurring during late gestation in a semi-synchronous manner in females. By birth, oocytes arrest in a modified diplonema, a unique stage called dictyate arrest, which is maintained until resumption of meiosis occurs at ovulation (Borum, 1961). Thus, cohorts of oocytes resume meiosis with each estrous/menstrual cycle, completing meiosis only at fertilization (Morelli and Cohen, 2005).

Studies described here reveal that Cntdl homozygous mutant females are sterile due to a failure to load MutLγ during pachynema of prophase I, resulting in an almost complete absence of chiasmata at metaphase I, similar to that seen for females lacking either Mlhl or Mlh3 (Kan et al., 2008; Woods et al., 1999). Cntdl mutant females have a dramatic decrease in primordial follicles starting soon after birth, whereas loss of Mlhl or Mlh3 results in normal folliculogenesis through adulthood (Edelmann et al., 1996; Lipkin et al., 2002). These subtle differences in outcomes for oocyte survival and subsequent folliculogenesis suggest that CNTD1 may play roles outside of the canonical CO designation

pathway, most likely involving its cyclin-independent regulation of meiotic cell cycle events (Gray et al., 2020).

Results

Oocytes from Cntd1^{-/-} female mice show a complete absence of class I COs

To determine the localization of CNTD1 in prophase I oocytes, we generated chromosome spreads from ovaries of mouse embryos at 18.5 days after coitum (dpc), which corresponds to the developmental time point during which most of the germ cells are in pachynema of prophase I (Borum, 1961; Hwang et al., 2018; Sun and Cohen, 2013). We utilized two lines of mice generated in our previous studies (Gray et al., 2020): the first bearing a null allele of *Cntd1*, referred to as *Cntd1*^{-/-}, and the second harboring a tandem FLAG and HA-tagged variant of Cntd1, referred to as Cntd1^{HA/HA}. The Cntd1^{HA} allele behaves much like the wild-type allele, and thus, for all our experiments, we crossed both alleles to generate one experimental mouse strain, using Cntd1HA/HA mice as our wild-type controls, CntdIHA/- mice as our heterozygous animals, and Cntdl-/- mice as our homozygous mutant test mice. Following chromosome spreading, oocyte nuclei were stained with antibodies against a component of the SC, SYCP3, and either the HA epitope for CNTD1 visualization (Fig. 1, A-C) or MLH1 for class I CO maturation (Fig. 1, E-G). We also performed colocalization of CNTD1 and MLH3 using the HA antibody and an anti-MLH3 antibody (Fig. S1, A-H). Cntd1HA/HA oocytes had on average 27 CNTD1HA foci, CntdlHA/- oocytes had an average of 26 foci, and as expected, Cntd1-/- oocytes did not show the presence of CNTD1^{HA} on chromosome spreads (Fig. 1 D and Table S1). Chromosome spread analysis of class I markers revealed abundant MLH1 foci at pachynema in both Cntd1HA/HA and CntdIHA/- oocytes (averaging 27 and 25 foci, respectively), but a complete absence of MLH1 foci in pachytene oocytes from Cntd1-/- females (Fig. 1 H and Table S1). Similar to CNTD1HA counts, the MLH1 counts observed in CntdlHA/- oocytes were statistically significantly decreased compared with those in CntdlHA/HA oocytes (Fig. 1 H and Table S1). There was no difference in the quantity of CNTD1HA foci compared with MLH1 foci in both CntdlHA/HA and CntdlHA/- oocytes (Fig. 1, I and J; and Table S1). The significant decline in both CNTD1^{HA} and MLH1 foci in Cntd1HA/- oocytes could be due to the dosage of Cntd1, which has been observed in other pro-CO factors such as HeilO and Rnf212 (Qiao et al., 2014; Reynolds et al., 2013). The absence of MLH1 indicates either that CNTD1 is acting upstream of MutLy or that CNTD1 is necessary for MutLy accumulation at sites of COs. Moreover, the absence of HA and MLH1 foci in Cntd1^{-/-} oocytes is consistent with our published work characterizing the function of CNTD1 in mammalian spermatogenesis (Gray et al., 2020).

To directly investigate the colocalization of CNTD1 and MutLy, we costained oocyte spreads with HA and MLH3. On average, ~89% and ~93% of CNTD1^{HA} foci were found to colocalize with MLH3 at pachynema in spreads from Cntd1^{HA/HA} and Cntd1^{HA/-} oocytes, respectively. Conversely, ~91% and ~87% of MLH3 foci localized with CNTD1^{HA} in Cntd1^{HA/HA} and Cntd1^{HA/-} oocytes, respectively (Fig. S1). The close colocalization pattern of CNTD1 with MLH3 lends evidence to the function of



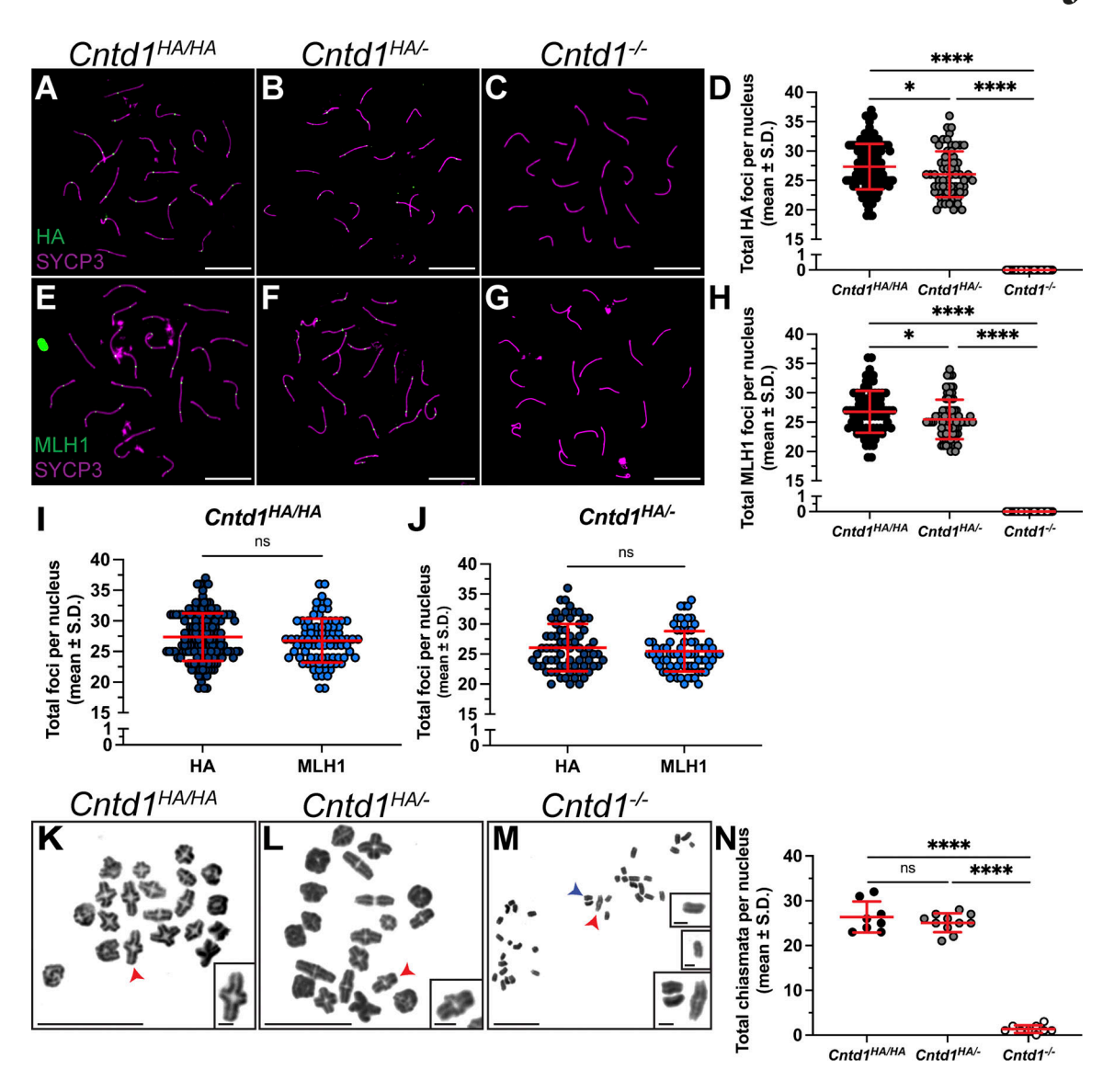


Figure 1. $Cntd1^{-/-}$ females lack class I COs and show a significant increase in univalent chromosomes. (A–C) Localization of CNTD1-HA (green) and SYCP3 (magenta) in pachytene oocytes from (A) $Cntd1^{HA/HA}$, (B) $Cntd1^{HA/-}$, and (C) $Cntd1^{-/-}$ 18.5 dpc fetuses using antibodies against each protein raised in rabbit and mouse, respectively. (E–G) Localization of MLH1 (green) and SYCP3 (magenta) in pachytene oocytes from (E) $Cntd1^{HA/HA}$, (F) $Cntd1^{HA/-}$, and (G) $Cntd1^{-/-}$ 18.5 dpc fetuses using antibodies against each protein raised in mouse and rabbit, respectively. (D) Quantification (average foci \pm SD) of HA foci in oocytes from $Cntd1^{HA/HA}$ (n = 157 nuclei; 27 ± 3.9), $Cntd1^{HA/-}$ (n = 66 oocytes; 26 ± 3.9), and $Cntd1^{-/-}$ (n = 47 oocytes; 0 ± 0) females. Statistical comparisons: $Cntd1^{HA/HA}$ and $Cntd1^{HA/-}$ and $Cntd1^{HA/-}$ and $Cntd1^{-/-}$: P < 0.0001, $Cntd1^{HA/-}$ and $Cntd1^{-/-}$: P < 0.0001, $Cntd1^{HA/-}$ and $Cntd1^{-/-}$: P < 0.0001, $Cntd1^{HA/-}$ and $Cntd1^{-/-}$: P < 0.0001. White scale bars represent 20 μ m. (I and J) Statistical comparison of HA and MLH1 foci in $Cntd1^{HA/HA}$ and $Cntd1^{HA/-}$ and $Cntd1^{HA/$

the former as a class I CO regulator. This result is also supported by the similar number of MLH1 and CNTD1 foci at pachynema (Fig. 1, D, H, and I).

CO maturation is disrupted in Cntd1-/- females

At the end of prophase I, COs manifest into physical linkages holding homologous chromosomes together, known as chiasmata.

Chiasma formation was normal in *Cntd1*^{HA/HA} and *Cntd1*^{HA/-} oocytes and was present on average at 26 and 25 chiasmata, respectively (red arrows, Fig. 1, K–N and Table S1). However, *Cntd1*^{-/-} oocytes showed a significant decline in chiasma formation compared with *Cntd1*^{HA/HA} and *Cntd1*^{HA/-} oocytes, resulting in an increase of univalent chromosomes (blue arrow, Fig. 1 M and Table S1). *Cntd1*^{-/-} oocytes retained on average 1.2



chiasmata per cell (red arrow, Fig. 1, M and N), reflecting an ~95% loss of COs, presumably indicative of a functional class II CO pathway, albeit at a slightly reduced rate to that seen in male meiosis (Holloway et al., 2008, 2014). Taken together, these results indicate that *Cntd1* is essential for class I CO formation, which is consistent with the model that CNTD1 is involved in regulating MLH1 placement, but not essential for class II CO formation, as evidenced by the persistence of a small number of residual chiasmata.

CNTD1 in the ovary is expressed at the same molecular weight as in the testis

Like its nematode ortholog, COSA-1, the predicted "full-length" isoform of CNTD1 was hypothesized to act as a cyclin due to the presence of three cyclin homology regions (Gray et al., 2020; Yokoo et al., 2012) (Fig. 2 A). Although COSA-1 has been shown to interact with CDK2 to facilitate CO designation in worms, immunoprecipitations from mouse testis lysate do not show evidence of an interaction between mammalian CNTD1 and COassociated CDK2, nor with any other cyclin-dependent kinase (Bondarieva et al., 2020; Gray et al., 2020). Western blot analysis of CNTD1HA showed a smaller-than-predicted CNTD1 protein of molecular weight ~ 30 kDa (compared with the predicted fulllength weight of 39.4 kDa), suggesting that a later translational start causes the loss of an N-terminal cyclin homology domain required for interaction with CDK2 (Gray et al., 2020). This smaller form of CNTD1 (CNTD1SF) is the only form of CNTD1 found in mouse spermatocytes or indeed in any tissue in male mice (Gray et al., 2020).

We first performed western blot analyses with whole testis lysates from our Cntd1 mutant and Cntd1HA-tagged mouse lines and probed with custom antibodies from Bondarieva et al. (2020), which were raised against the C terminus of CNTD1 between amino acids Cys126 and Thr249 (Fig. 2, A-C and Fig. S2 A). Only the \sim 30 kDa CNTD1 and slightly larger CNTD1^{HA} bands were detected with both custom antibodies in our Cntdl mouse lines (pink and blue arrows, Fig. 2, B and C). We raised a custom CNTD1 antibody against residues 86-334 and detected a CNTD1 band migrating at ~30 kDa in C57BL/6J control testis lysate but not in Cntd1-/-, confirming that endogenous mouse CNTD1 runs at a band size that is smaller than the predicted full-length protein (Fig. S2 D). To test whether CNTD1SF is conserved in other mammals, we probed testis lysates from cat, dog, horse, and human. Although there is some variation in size, CNTD1 runs at a similar molecular weight in all these lysates, indicating that CNTD1SF is the predominant protein localizing to mammalian spermatocytes. Interestingly, the CNTD1SF band is absent in one human testis sample ("human 1") that did not contain recoverable spermatocytes from a patient with nonobstructive azoospermia, supporting the specificity of this band (Fig. S2, D-F).

Next, we tested whether CNTD1 is present at the same molecular weight in mouse oocytes or whether the full length is present, possibly providing an explanation for the observed sexual dimorphism in prophase I outcomes between males and females. We performed a western blot analysis with whole testis lysate and whole ovary lysate from *CntdIHA/HA* mice at 18.5 dpc

using an HA antibody as a proxy for CNTD1. We detected a specific \sim 30 kDa CNTD1 band in the whole ovary lysate, which matched the band size of CNTD1^{SF} from the whole testis lysate. This band was not present in $Cntdl^{-/-}$ whole testis lysate samples, confirming the specificity of the antibody (blue arrows, Fig. 2 C).

To further confirm the size of CNTD1 present in oocytes, we enriched for CNTD1-HA by performing a co-immunoprecipitation with antibodies against HA to isolate CNTD1-HA from fetal ovary cell lysates collected at 18.5 dpc and then probed via western blot with anti-HA antibody. CNTD1-HA was present in the IP elutions at the same molecular weight (~30 kDa) in oocytes ($Cntdl^{HA/HA}$ \circ) as in spermatocytes ($Cntdl^{HA/HA}$ \circ) (blue arrows, Fig. 2 D). We did not find HA-tagged CNTD1 in the fetal whole ovary lysate from C57BL/6J females (C57BL/6J ♀). A nonspecific band at ~40 kD is present in both the HA samples and the C57BL/6J control (black asterisks). The slightly slower migration of the CNTD1-HA band in the ovary lysate IP elution compared with the testis lysate elution is likely a result of the gel running unevenly, as evidenced by the identically sized bands shown previously (Fig. 2 C). Taken together, these data show that CNTD1 is present in both spermatocytes and oocytes at a size that is smaller than the predicted full-length form and that this smaller isoform of CNTD1 may be incapable of interacting in vivo with any known spermatocyteassociated CDK. We propose a model, therefore, in which the endogenous CNTD1 protein lacks a key cyclin homology domain, suggesting that CNTD1 is functioning via a cyclin-independent mechanism in mammalian oocytes.

The absence of *Cntd1* results in sterility and loss of primordial follicles

In males, disruption of factors essential for class I CO formation and distribution results in complete sterility and manifests in a phenotype characterized by gross morphological defects in gonadal tissues, including a significant decrease in testis size coupled with a significant loss of meiocytes and loss of postmeiotic cells in testis tissue sections (Bondarieva et al., 2020; Gray et al., 2020; Holloway et al., 2014). Morphological effects appear to be bifurcated in females, where there are two distinct phenotypes. The first is observed in mutants that affect early DSB repair (Dmc1, Msh4/5) events and leads to a significant reduction in ovarian size and lack of folliculogenesis resulting from disruption of meiotic prophase prior to pachynema (Edelmann et al., 1999; Kneitz et al., 2000; Pittman et al., 1998; Yoshida et al., 1998). The second phenotypic category is characterized by later prophase I (Mlh1/3, Hei10) disruption from pachynema onward, resulting in normal ovarian morphology and follicle composition (Bondarieva et al., 2020; Edelmann et al., 1996; Ward et al., 2007). Due to the accumulation of CNTD1 in pachynema and its colocalization with other pro-CO factors, we hypothesized a similar phenotype to the latter.

To explore the consequences of CNTD1 dysfunction in the oocyte for ovarian development and folliculogenesis, we investigated fertility, ovarian morphology, and follicle populations. $Cntd1^{-/-}$ females were unable to produce litters after ~ 3 mo housed with a $Cntd1^{HA/HA}$ male (Fig. S1 I), confirming that these



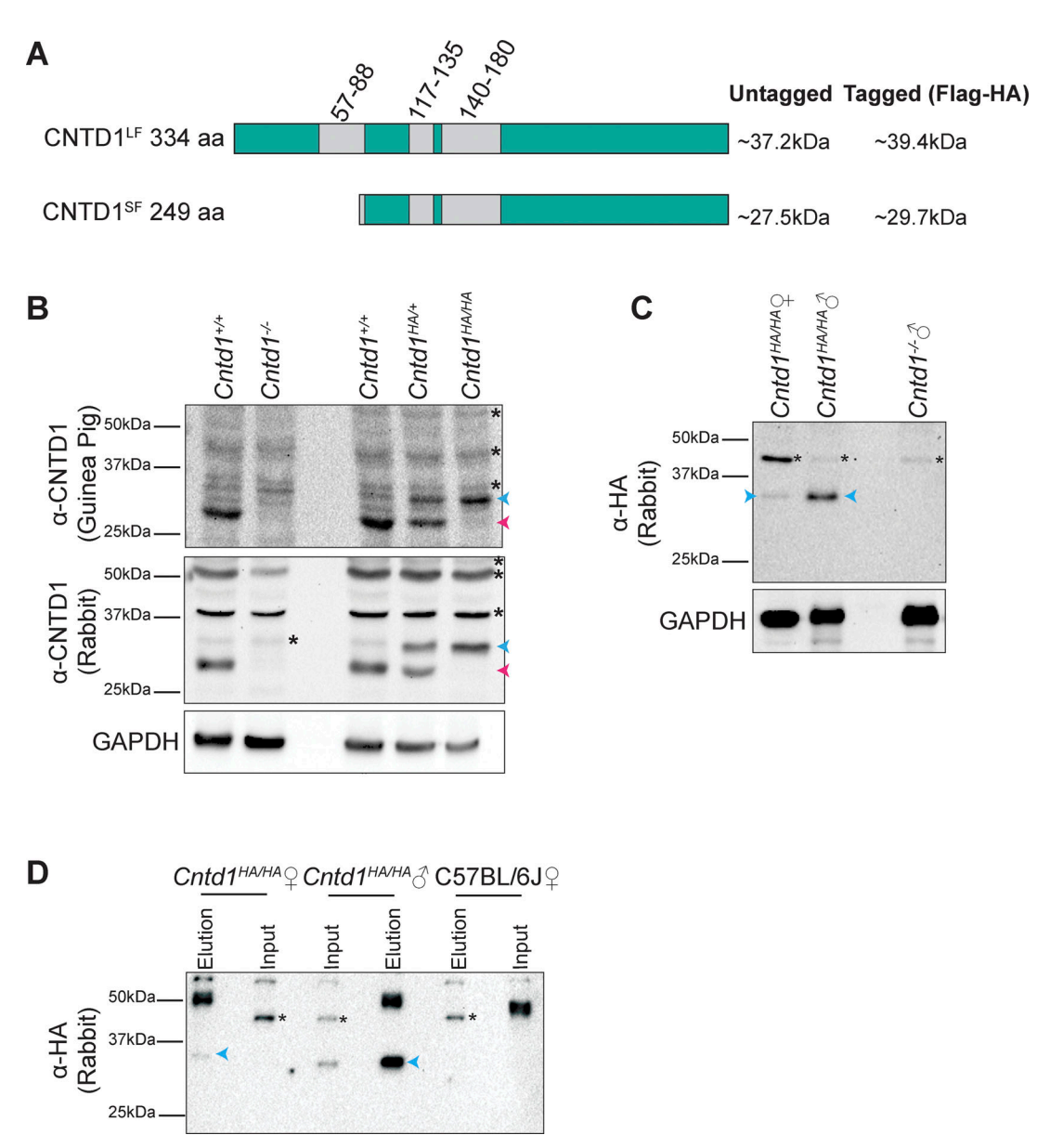


Figure 2. **CNTD1 exists as a short form in fetal oocytes.** Western blot and co-immunoprecipitation with custom CNTD1 and anti-HA antibodies in fetal ovary and adult testis lysate. **(A)** In silico prediction of the long form and short form of CNTD1 with cyclin homology domains in light gray and predicted molecular weight with and without Flag-HA epitope tags to the left of the diagram. **(B)** Western blots against whole testis lysates from Cntd1 mutant and $Cntd1^{HA}$ mouse lines probed with custom CNTD1 antibodies from Bondarieva et al. (2020) run on a 10% SDS-PAGE gel. **(C)** Western blot against whole ovary lysate from 18.5 dpc ovaries from $Cntd1^{HA/HA}$ fetuses (~40 ovaries) and whole testis lysate from $Cntd1^{HA/HA}$ and $Cntd1^{-/-}$ adult males run on a 10% SDS-PAGE gel, probed with the anti-HA antibody. **(D)** Western blot against HA from IPs performed in the 18.5 dpc whole ovary lysate from $Cntd1^{HA/HA}$ and C57BL/6J females, and the whole testis lysate from $Cntd1^{HA/HA}$ adult males on a 10% SDS-PAGE gel, probed with the anti-HA antibody. Approximately 40–100 ovaries from $n \ge 20$ fetuses were utilized per IP sample. Black asterisks denote nonspecific bands. Pink arrows show the predicted molecular weight of the untagged short form of CNTD1, and blue arrows indicate the predicted molecular weight of the short form of CNTD1 with the dual FLAG-HA epitope tags. Uncropped blots of those in this figure can be found in Fig. S2. Source data are available for this figure: SourceData F2.

animals are infertile. $Cntdl^{HA/-}$ females produced on average one fewer offspring compared with $Cntdl^{HA/HA}$ females (Fig. S1 I). To determine whether ovaries from $Cntdl^{-/-}$ females exhibit morphological phenotypes characteristic of early or late prophase I disruption, we quantitated the ovarian follicular composition from prepubertal postnatal day (PND) 1, 14, 28, and adult (8–12 wk old) females ($n \ge 3$ for each time point), documenting the follicular stages from primordial (early) follicles through antral (late preovulatory) follicles. Primordial follicles contain the

CNTD1 is critical for meiosis in female mice

dictyate arrested oocyte surrounded by one layer of granulosa cells and represent the finite pool of germ cells and reproductive potential of the individual. Maturation to primary through antral follicles is only induced upon sexual maturity, and these follicle types are characterized by layers of granulosa and theca cells, which secrete hormones that facilitate this maturation process (Fig. 3 Q) (Epifano and Dean, 2002). Prematurely exhausted primordial follicle pools can be indicative of defects in oogenesis prior to the formation of primordial follicles.



At PND1, the total number of oocytes in Cntd1^{HA/HA}, Cntd1^{HA/-}, and *Cntd1*^{-/-} was reduced but not statistically changed between CntdlHA/HA and CntdlHA/-, CntdlHA/HA and Cntdl-/-, and CntdlHA/and Cntd1-/- (Fig. 3, A-D and Table S2). We observed a significant decrease in primordial-stage follicles in Cntd1-/- ovaries compared with Cntd1HA/HA and Cntd1HA/- ovaries in PND14 females (Fig. 3, E-H and Table S2). There was no difference in the number of primordial follicles between Cntd1HA/HA and Cntd1HA/animals (Fig. 3 H and Table S2). Secondary and antral-staged follicles were unchanged in CntdlHA/HA, CntdlHA--, and Cntdl-/ovaries (Fig. 3 H and Table S2). At PND28, we observed no change in the average number of primordial follicles found in CntdlHA/HA compared with CntdlHA/- ovaries, but there was a decrease in primordial follicles in Cntd1-/- compared with Cntd1^{HA/HA} ovaries (Fig. 3, I-L and Table S2). The average number of primary follicles did not differ in ovaries from CntdlHA/HA animals compared with Cntdl-/-, but the number of primary follicles was decreased in Cntd1-/- compared with Cntd1^{HA/-} (Fig. 3 L and Table S2). There was no difference in the number of primary follicles between Cntd1HA/HA and Cntd1HA/ovaries (Fig. 3 L and Table S2). We observed no difference in the quantity of secondary and antral follicles in any of the genotypes at PND28 (Fig. 3 L and Table S2). In adult Cntd1-/- ovaries, we observed a significant decrease in all follicle types in comparison with Cntd1^{HA/HA} and Cntd1^{HA/-} (Fig. 3 P and Table S2). There were no significant differences between total follicle numbers in CntdlHA/HA and CntdlHA/- ovaries for any of the follicle types (Fig. 3 P and Table S2).

Taken together, these data suggest that the absence of *Cntd1* results in a similar yet distinct ovarian phenotype to the late CO designation mouse mutants, in which ovarian morphology is unaltered, but there is a dramatic loss of follicles not seen in other late CO designation mutants. The primordial follicles present at PND1 can progress through folliculogenesis, but the oocytes contained within them are inviable. Importantly, the quality checkpoints in oocytes appear to be particularly leaky compared with spermatocytes, which is evident from oocytes with ~5% COs reaching the end of prophase I (Bondarieva et al., 2020; Condezo et al., 2024; Ward et al., 2007). Thus, this raised the question of other defects that *Cntd1*-/- oocytes harbored.

Cntd1-/- oocytes exhibit aberrant markers of DSBs

Due to the premature loss of primordial follicles in $CntdI^{-/-}$ ovaries, we were interested in investigating the quality control mechanism by which these oocytes were being lost. Incomplete synapsis of homologous chromosomes and unrepaired DSBs during meiotic prophase I in oocytes trigger the synapsis and DSB checkpoints (e.g., dual-checkpoint model), leading to oocyte apoptosis in the absence of sufficient repair (Bolcun-Filas et al., 2014; Ravindranathan et al., 2022; Rinaldi et al., 2017, 2020). To assess whether early DSB repair and recombination events are affected in $CntdI^{-/-}$ oocytes, we used antibodies against RAD51 and γ H2A.X to stain spread chromosomes in pachytene-staged oocytes from 18.5 dpc fetuses in all CntdI genotypes (Figs. 4 and 5). All genotypes showed canonical staining patterns in which RAD51 accumulated as expected in zygotene-staged oocytes (Fig. 4, D-F) and was almost completely absent by pachynema

(Fig. 4, G–I), indicating normal progression of DSB repair past the strand invasion stages. Upon analysis of RAD51 foci at pachynema, however, *CntdI*^{-/-} showed a modest but statistically significant increase of one RAD51 focus in comparison with *CntdI*^{HA/HA} oocytes (Fig. 4 M and Table S1). There was no change in the number of foci between *CntdI*^{HA/HA} and *CntdI*^{HA/-} (Fig. 4 M and Table S1).

We next investigated γ H2A.X, which serves as another marker of unrepaired breaks. In its unphosphorylated state as H2A.X, it is a target of surveillance kinases such as ATR and ATM in the DNA damage response pathway (Collins et al., 2020). We measured the nuclear intensity of the γ H2A.X signal in pachytene oocytes from $Cntd1^{-/-}$ and $Cntd1^{HA/HA}$ embryos and observed that the former was markedly reduced compared with the latter (Fig. 5, A, C, and D; and Table S1). γ H2A.X was also reduced in $Cntd1^{HA/-}$ oocytes compared with $Cntd1^{HA/HA}$ littermate controls (Fig. 5, A, B, and D; and Table S1).

Although there was a statistically significant increase in the number of RAD51 foci in Cntd1 mutant pachynema-staged oocytes, this increase is most likely not sufficient to trigger the DSB portion of the dual checkpoint, due to previous reports indicating that oocytes can withstand $\sim \! \! 10$ unrepaired DSBs before induction of the checkpoint (Ravindranathan et al., 2022). Coupled with the decrease in $\gamma H2A.X$ intensity in Cntd1 mutants, which we would expect would increase if there were issues in DSB repair, it leads us to propose that although DSB repair markers are statistically different between Cntd1 mutants and their wild-type counterparts, this difference is likely not adequate to contribute to the loss of oocytes lacking CNTD1 in prophase I.

Cntd1-/- oocytes have altered SYCP1 and SYCP3 patterning

Previous work from our laboratory showed that spermatocytes from Cntd1-/- males show no overt defects in SC formation and homolog synapsis (Gray et al., 2020; Holloway et al., 2014). To investigate whether such defects in SC assembly could explain the early loss of primordial follicles in *Cntd1*^{-/-} females, we analyzed synapsis in prophase I oocytes at 17.5 and 18.5 dpc using antibodies against the SC: SYCP1, which marks the transferase filaments of the SC and is a marker of synapsis, and SYCP3. We assessed SC assembly and maintenance (at least three biological replicates, quantifying the first 100 cells per slide-400-500 oocytes in total per genotype) by characteristic SYCP1/3 colocalization (synapsis) patterning. We distinguished oocytes based on previously established criteria: leptotene ("firework-like" patterning of only SYCP3), zygotene (partial synapsis and "forks" at the end of SYCP3 filaments with no SYCP1 colocalization, and no "bubbles," concurrently present with longer SYCP3 filaments), pachytene (full colocalization of SYCP1/3), diplotene (bubbles with just SYCP3, with or without forks, or full repulsion of SYCP3 filaments without colocalization of SYCP1, and also present with shorter filaments when marked with SYCP3) (see Materials and methods and examples provided in Fig. S3 M) (Goetz et al., 1984; Morelli et al., 2008; Speed, 1982). Defects in the ability of these proteins to assemble properly result in quality control checkpoint activation and subsequent apoptosis at the end of prophase I (Hamer et al., 2008; Yuan et al., 2000).



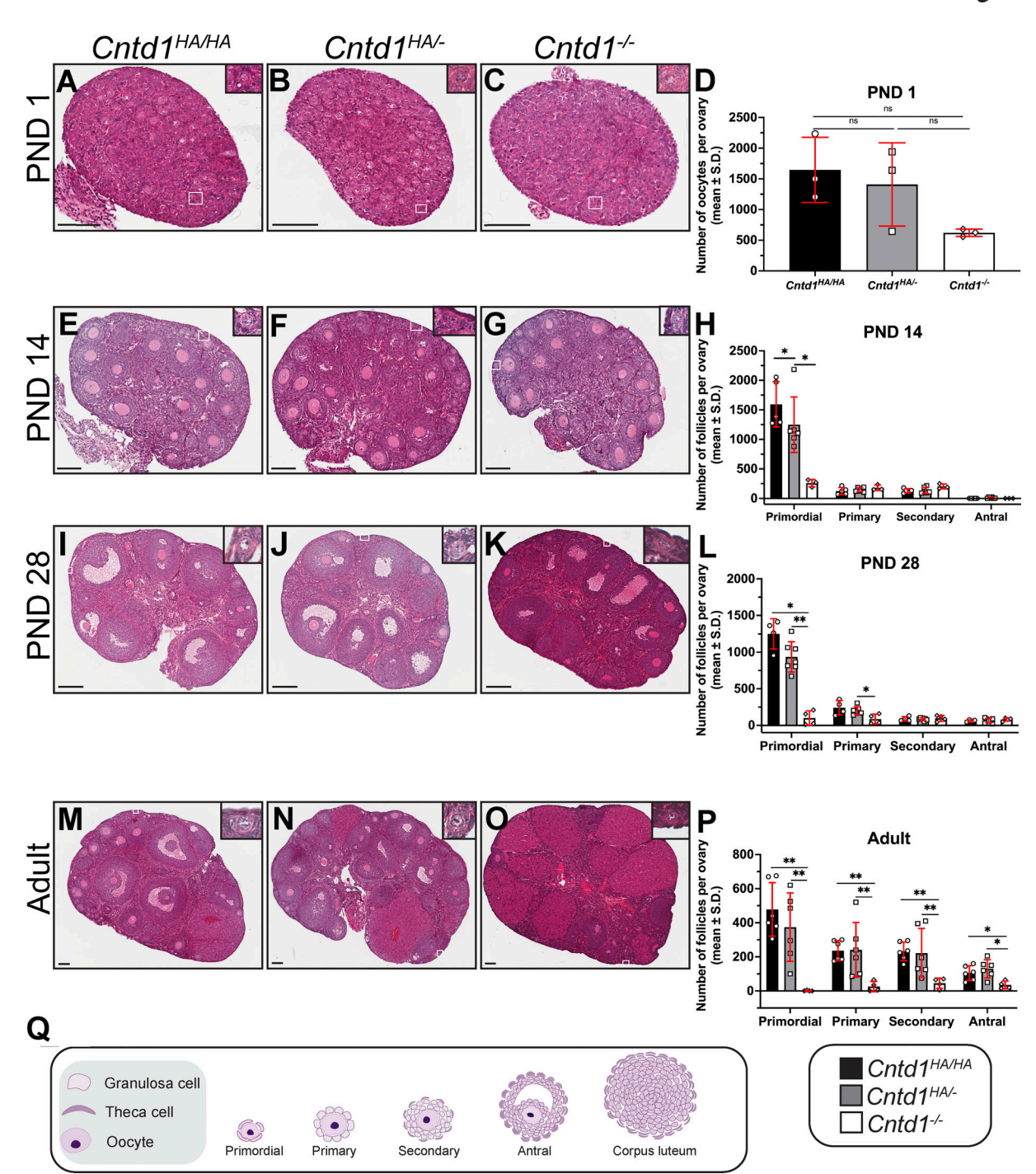


Figure 3. Ovarian histology in Cntd1^{HA/HA}, Cntd1^{HA/-}, and Cntd1^{-/-} females at different postnatal ages reveals a significant increase in the loss of primordial follicles. (A–O) Histological sections of ovaries from Cntd1^{HA/HA}, Cntd1^{HA/-}, and Cntd1^{-/-} female mice at PND1 (A–C), PND14 (E–G), PND28 (I–K), and adult (8–10 wk) (M–O). Examples of primordial follicles present are in the upper right-hand corner, with the specific follicle highlighted by a white box in the representative image. Paraffin-embedded tissues were sectioned at 5 μm and stained with hematoxylin and eosin. Scale bars are equal to 100 μm. (P) Quantification of primordial, primary, secondary, and antral follicles in ovaries at (D) PND1 (statistical analysis: Cntd1^{HA/HA} and Cntd1^{HA/-}: P > 0.9999, Cntd1^{HA/HA} and Cntd1^{-/-}: P = 0.1, Cntd1^{HA/-} and Cntd1^{-/-}: P = 0.0238; primary follicles: Cntd1^{HA/HA} and Cntd1^{HA/-}: P = 0.4589, Cntd1^{HA/-} and Cntd1^{-/-}: P = 0.1429, Cntd1^{HA/-} and Cntd1^{-/-}: P = 0.5476; secondary follicles: Cntd1^{HA/HA} and Cntd1^{HA/-}: P = 0.9576, Cntd1^{HA/HA} and Cntd1^{-/-}: P = 0.0714, Cntd1^{HA/-} and Cntd1^{-/-}: P = 0.1905; antral follicles: Cntd1^{HA/HA} and Cntd1^{HA/-}: P = 0.1775, Cntd1^{HA/HA} and Cntd1^{-/-}: P = 0.0286, Cntd1^{HA/-} and Cntd1^{-/-}: P = 0.06485, Cntd1^{HA/HA} and Cntd1^{-/-}: P = 0.06485, Cntd1^{HA/HA} and Cntd1^{-/-}: P = 0.06485, Cntd1^{HA/HA} and Cntd1^{-/-}: P = 0.6848, Cntd1^{HA/HA} and Cntd1^{-/-}: P = 0.6848, Cntd1^{HA/HA} and Cntd1^{-/-}: P = 0.0999, Cntd1^{HA/HA} and Cntd1^{HA/-}: P = 0.6848, Cntd1^{HA/HA} and Cntd1^{-/-}: P = 0.0999, Cntd1^{HA/HA} and Cntd1^{HA/-}: P = 0.6848, Cntd1^{HA/HA} and Cntd1^{-/-}: P = 0.0999, Cntd1^{HA/HA} and Cntd1^{HA/-}: P = 0.6848, Cntd1^{HA/HA} and Cntd1^{-/-}: P = 0.0999, Cntd1^{HA/HA} and Cntd1^{HA/-}: P = 0.6999, Cntd1^{HA/HA} and Cntd1^{HA/-}: P = 0.6999, Cntd1^{HA/HA} and Cntd1^{HA/-}: P = 0.0999, Cntd1^{HA/HA} and Cntd1^{HA/-}: P = 0.0999, Cntd1^{HA/HA} and Cntd1^{HA/-}: P = 0.0999, Cntd1^{HA/HA} and Cntd1^{HA/-}: P = 0.09999, Cntd1^{HA/HA} and Cntd1^{HA/-}: P = 0.09999, C



0.0095, $Cntd1^{HA/-}$ and $Cntd1^{-/-}$: P = 0.0095; secondary follicles: $Cntd1^{HA/+A}$ and $Cntd1^{HA/-}$: P = 0.5087, $Cntd1^{HA/+A}$ and $Cntd1^{-/-}$: P = 0.0095, $Cntd1^{HA/-}$ and $Cntd1^$

We analyzed the distribution of prophase I substages in all *CntdI* genotypes at 17.5 and 18.5 dpc, and found altered proportions in *CntdI*^{-/-} oocytes at both time points, which were not consistent with previous reports of prophase I substaging distribution (Fig. 6 and Fig. S3) (Borum, 1961; Speed, 1982). We

could not detect leptotene-staged cells in *Cntd1*^{HA/HA} oocytes at 17.5 dpc, but this was attributed to the random selection method for quantitation (Materials and methods) coupled with the very low abundance of leptotene cells observed during prophase I (Speed, 1982). Approximately 10% and 25% (18.5 and 17.5 dpc) of

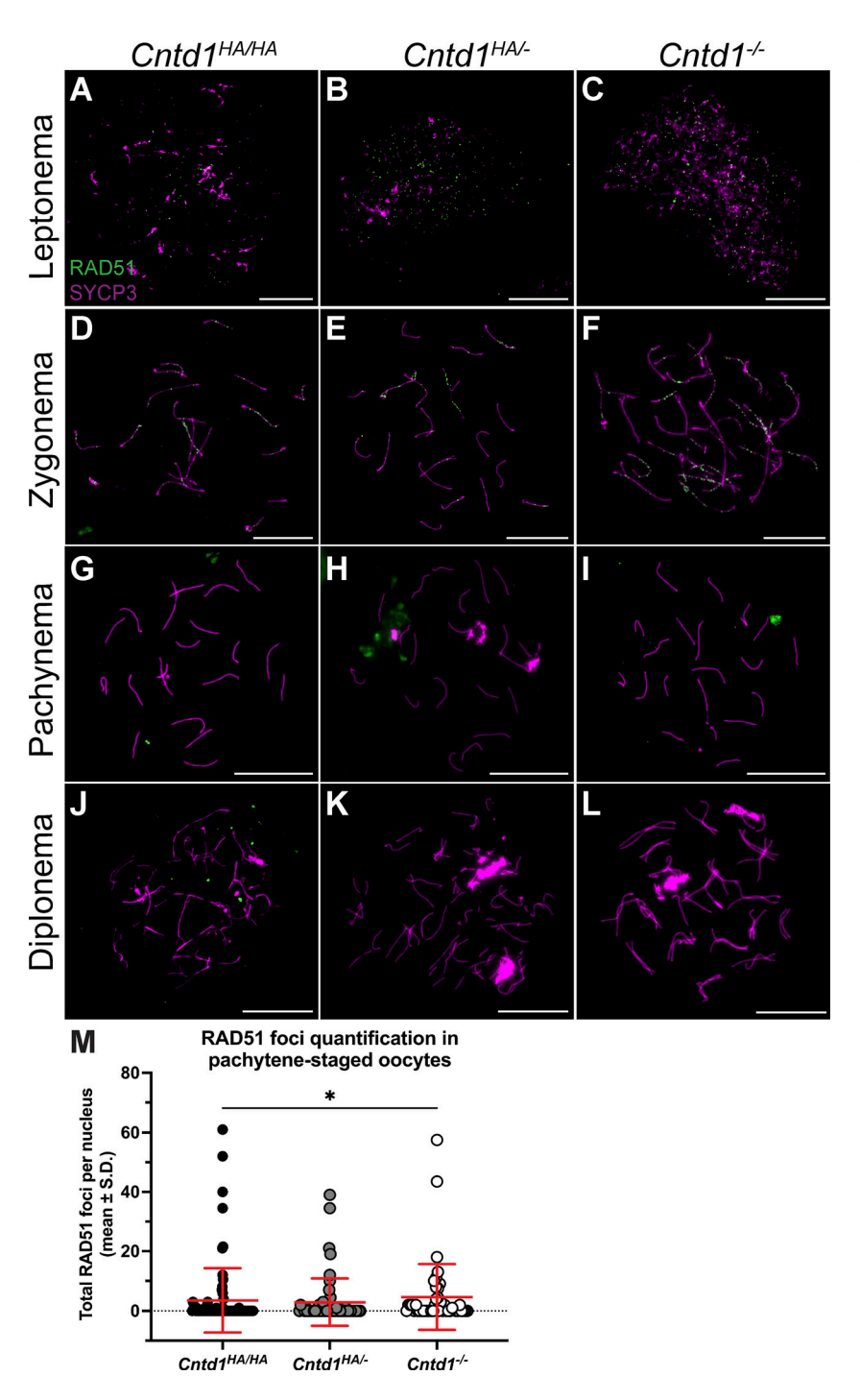


Figure 4. Early DSB repair in Cntd1-/- oocytes is normal. (A-L) Localization of RAD51 (green) and SYCP3 (magenta) on chromosome spreads from Cntd1^{HA/HA}, Cntd1^{HA/-}, and Cntd1^{-/-} oocytes at leptonema (A-C), zygonema (D-F), pachynema (G-I), and diplonema (J-L), using antibodies against each protein raised in rabbit and mouse, respectively. (M) Quantification of RAD51 (average foci ± SD) in pachytene-staged cells from 18.5 dpc ovaries for $Cntd1^{HA/HA}$ (n = 83 nuclei; 3.5 ± 11), $Cntd1^{HA/-}$ (n = 51 nuclei; 2.9 \pm 7.9), and Cntd1^{-/-} (n = 44 nuclei; 4.7 \pm 11). Statistical analysis: Cntd1^{HA/HA} and Cntd1^{HA/-}: P = 0.7701, Cntd1^{HA/HA} and Cntd1^{-/-}: P = 0.0173, Cntd1^{HA/-} and $Cntd1^{-/-}$: P = 0.0555. $n \ge 3$ pairs of ovaries were used. Pachynema-staged oocytes were determined using SYCP3 (absence of forks or bubbles). Mean and standard deviation lines are in red. White scale bars are equal to 20 µm. A Mann-Whitney test was utilized to test for statistical significance. P values are as follows: *P < 0.05, **P < 0.001, ***P < 0.0002, ****P < 0.0001.



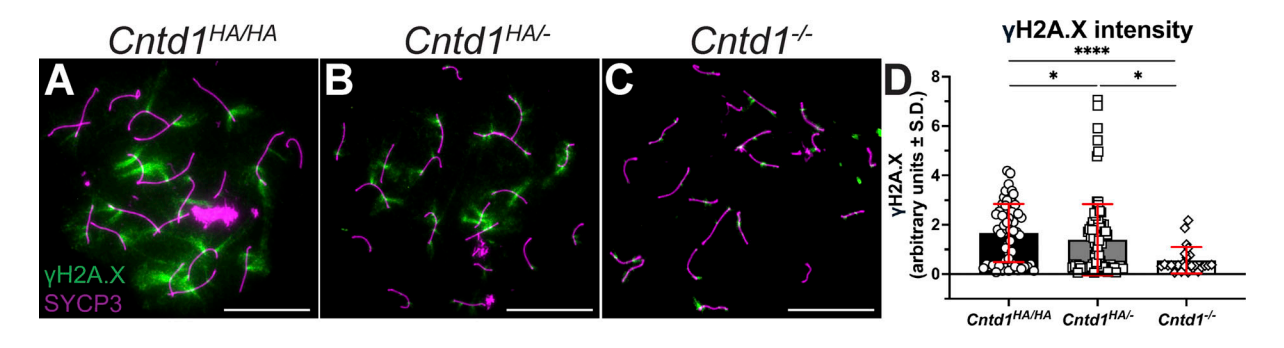


Figure 5. **γH2A.X intensity is reduced in** *Cntd1*^{-/-} **oocytes. (A-C)** Localization of γH2A.X (A-C) with SYCP3 (magenta) on chromosome spreads from *Cntd1*^{HA/HA}, *Cntd1*^{HA/-}, and *Cntd1*^{-/-} oocytes from 18.5 dpc ovaries at pachynema. **(D)** Quantification of the intensity of γH2A.X normalized to DAPI in pachytene-staged cells (mean intensity in arbitrary units ± SD) for *Cntd1*^{HA/HA} (n = 60 nuclei; 1.7 ± 1.2), *Cntd1*^{HA/-} (n = 94 nuclei; 1.4 ± 1.4), and *Cntd1*^{-/-} (n = 24 nuclei; 0.56 ± 0.54). Statistical analysis: *Cntd1*^{HA/HA} and *Cntd1*^{HA/-}: P = 0.0315, *Cntd1*^{HA/HA} and *Cntd1*^{-/-}: P = 0.0003, *Cntd1*^{HA/-} and *Cntd1*^{-/-}: P = 0.0241. $n \ge 3$ fetuses were used, and data were analyzed using the mean and standard deviation lines in red. White scale bars are equal to 20 μm. A Mann–Whitney test was utilized to test for statistical significance. P values are as follows: *P < 0.05, **P < 0.001, ***P < 0.0002, ****P < 0.0001.

Cntd1HA/HA oocytes were observed at zygonema compared with an increased number of zygotene oocytes in Cntd1-/- females at 17.5 dpc (~55%) but not 18.5 dpc (~7%). An alteration in substages was also observed in the frequency of pachytene-staged oocytes, with high numbers of pachytene-staged oocytes in CntdI^{HA/HA} females at both ages (~70%), and considerably lower numbers of pachytene cells in *Cntd1*^{-/-} females: ~13% (18.5 dpc) and \sim 27% (17.5 dpc). Diplotene-staged cells were also altered in their frequency, lower in Cntd1HA/HA females (~21% at 18.5 dpc and \sim 5% at 17.5 dpc) and higher in Cntd1^{-/-} females (\sim 79% at 18.5 dpc and ~16% at 17.5 dpc) (Fig. 6 M). Cntd1HA/- oocytes had a comparable distribution to Cntdl^{HA/HA} for both time points (Fig. 6 M). A chi-square analysis confirmed the difference in the distribution of prophase I substages (zygonema through diplonema) between Cntd1 genotypes at both 18.5 and 17.5 dpc time points (Fig. 6 M). Taken together, the altered prophase I substage proportions of oocytes in 17.5 and 18.5 dpc in Cntd1-/females indicate that CNTD1 has a role in regulating the maintenance of synapsis between homologous chromosomes, wherein, when synapsis is achieved in pachynema, it is not properly maintained and likely triggers the synapsis checkpoint, which is directly correlated with the decrease in primordial follicles starting shortly after birth and an increase in TUNELpositive cells shown with in situ analysis (Figs. 3 and S5).

Our previous work showed that CNTD1 interacts with components of the SKP1-Cullin-F-box (SCF) complex, and *Cntd1* mutant spermatocytes show a prophase I-to-metaphase I transition defect (Gray et al., 2020), similar to *Skp1cKO* mutants (Guan et al., 2020). SKP1, a component of the SCF E3 ubiquitin ligase complex that is essential for cell cycle progression during mouse meiosis (Guan et al., 2020, 2022), has been shown to be essential for synapsis and for the removal of HORMAD1/2 in mammalian oocytes and spermatocytes (Chotiner et al., 2023; Guan et al., 2022). We next investigated the localization of SKP1 in our *Cntd1* strains. In *Cntd1* HA/HA oocytes, we observed normal SKP1 localization to SCs; however, this localization appeared to be drastically reduced in *Cntd1*-/- oocytes (Fig. 7, A-C). We next measured the intensity of SKP1 in *Cntd1* oocytes and observed that compared with *Cntd1* HA/HA and *Cntd1* HA/-, *Cntd1*-/- showed a

significant reduction in the intensity of SKP1 (Fig. 7 D and Table S1).

Colocalization of SYCP1 and SYCP3 confirms that synapsis occurs without CNTD1. Considering the altered ratios of prophase I substages, particularly between pachynema and diplonema, we assessed HORMAD1, the synapsis checkpoint regulator (Kogo et al., 2012; Shin et al., 2013). We used a binary system and found a marked increase in HORMAD1 retention in Cntd1-/-oocytes (Materials and methods) (Fig. 7, E-H and Table S1). These results support previous reports that the SCF complex targets HORMAD1 for degradation and removal from synapsed regions of the SC (Chotiner et al., 2023; Guan et al., 2020, 2022) and suggest a role of CNTD1 in regulating SKP1 localization to SCs in oocytes.

To determine whether synapsis and DSB repair defects arise before 18.5 dpc, we examined 17.5 dpc oocytes. We hypothesized that if the pachytene checkpoint is activated, there would be differences between Cntdl^{HA/HA} and Cntdl^{-/-} oocytes at this time point. Despite no difference in DSB and ssDNA markers (γH2A.X, RAD51, and RPA2, respectively) between Cntdl^{HA/HA} and Cntdl^{-/-} oocytes, Cntdl^{-/-} showed persistent HORMAD1 and reduced SKP1, mirroring the 18.5 dpc findings (Fig. S4 and Table S3). Together, these results demonstrate that loss of Cntdl results in defects in DSB repair, aberrant prophase I progression, and disrupted HORMAD1 dynamics in pachytene-staged oocytes, with the latter being sufficient to trigger the pachytene checkpoint and cause significant loss of oocytes (Fig. 3).

Ablation of CHK1 and CHK2 rescues oocyte loss in Cntd1^{-/-} ovaries

DSB repair and synapsis are carefully monitored throughout prophase I through the action of the checkpoint surveillance kinases ATR and ATM (Huang and Roig, 2023; Martínez-Marchal et al., 2020; Ravindranathan et al., 2022). These kinases activate CHK1 and CHK2, respectively, in response to DNA damage (BolcunFilas et al., 2014; Chen et al., 2012; Huang and Roig, 2023; Martínez-Marchal et al., 2020; Rinaldi et al., 2017, 2020). Meiotic mutants with an exhausted ovarian reserve phenotype could be rescued by ablating CHK1 and/or CHK2



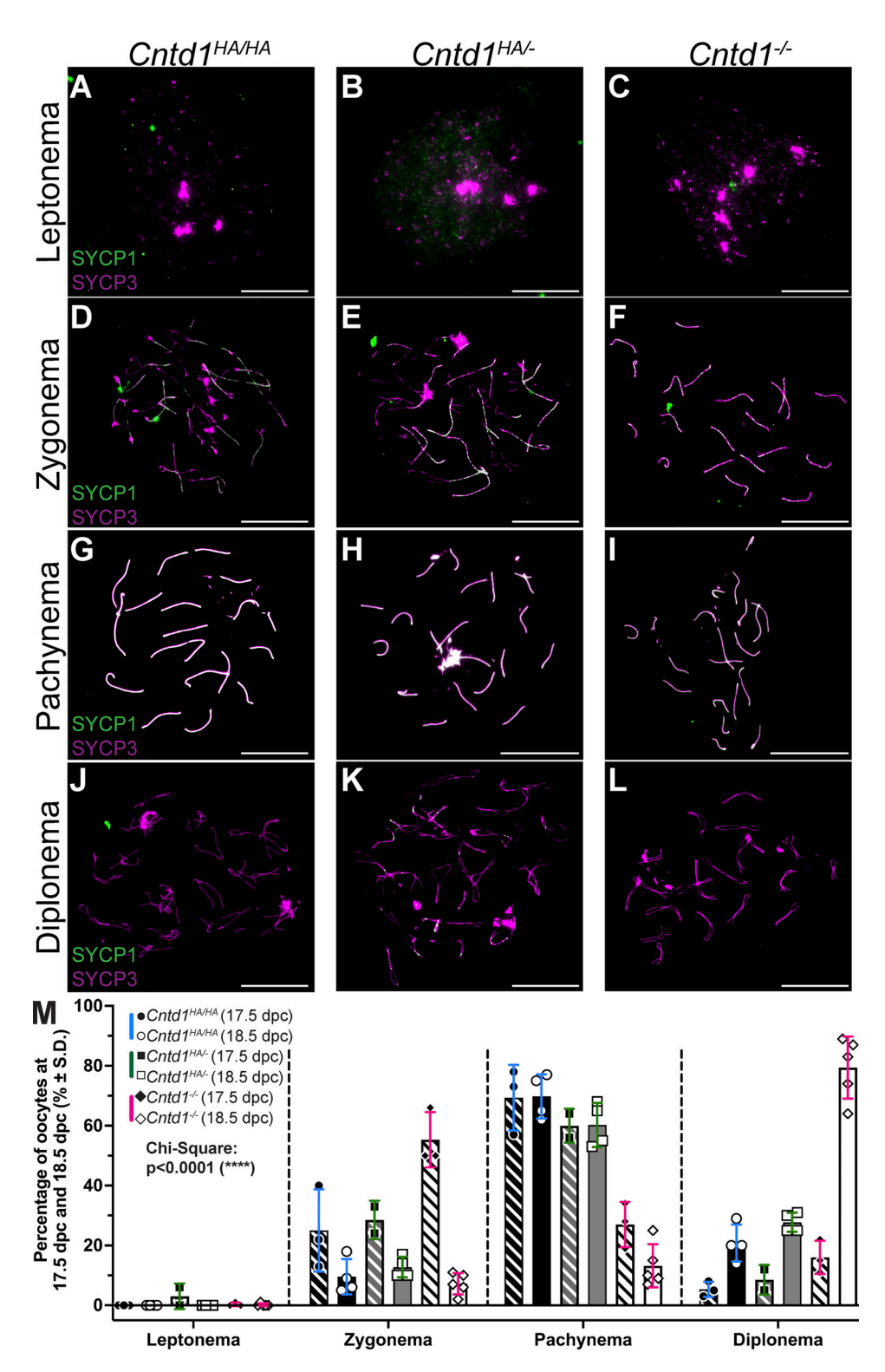


Figure 6. Progression through prophase I in Cntd1-/- oocytes is altered. (A-L) Localization of SYCP1 (green) and SYCP3 (magenta) on chromosome spreads from Cntd1^{HA/HA} (circles with blue error bars), Cntd1^{HA/-} (squares with green error bars), and Cntd1^{-/-} (diamonds with pink error bars) oocytes at leptonema (A-C), zygonema (D-F), pachynema (G-I), and diplonema (J-L), using antibodies against each protein raised in rabbit and mouse, respectively. (M) Analysis of prophase I substages in 17.5 and 18.5 dpc Cntd1^{HA/HA} (circles), Cntd1^{HA/-} (squares), and Cntd1^{-/-} (diamonds) oocytes. The average percentage was calculated as the sum (across biological replications) per substage divided by the total number of cells per genotype (e.g., 50 pachytene-staged oocytes divided by 400 total oocytes). For 17.5 dpc, oocyte prophase I substage distribution (representative images are in Fig. S3) was as follows: leptonema, (average %: Cntd1^{HA/HA}: 0%; Cntd1^{HA/-}: 3%; Cntd1^{-/-}: 0%), zygonema (D–F) (Cntd1^{HA/HA}: 25%; Cntd1^{HA/-}: 29%; Cntd1^{-/-}: 55%), pachynema (Cntd1^{HA/HA}: 69%; Cntd1^{HA/-}: 60%; Cntd1^{-/-}: 27%) (G-I), and diplonema (J-L) (Cntd1^{HA/HA}: 5%; Cntd1^{HA/-}: 9%; Cntd1^{-/-}: 16%). For 18.5 dpc, the following distributions were observed: leptonema (average %: Cntd1^{HA/HA}: 0%; Cntd1^{HA/-}: 0%; Cntd1^{HA/-}: 0%; Cntd1^{HA/-}: 70%; Cntd1^{HA/-}: 10%; Cntd1^{HA/-}: 10%

Wood et al. Journal of Cell Biology CNTD1 is critical for meiosis in female mice



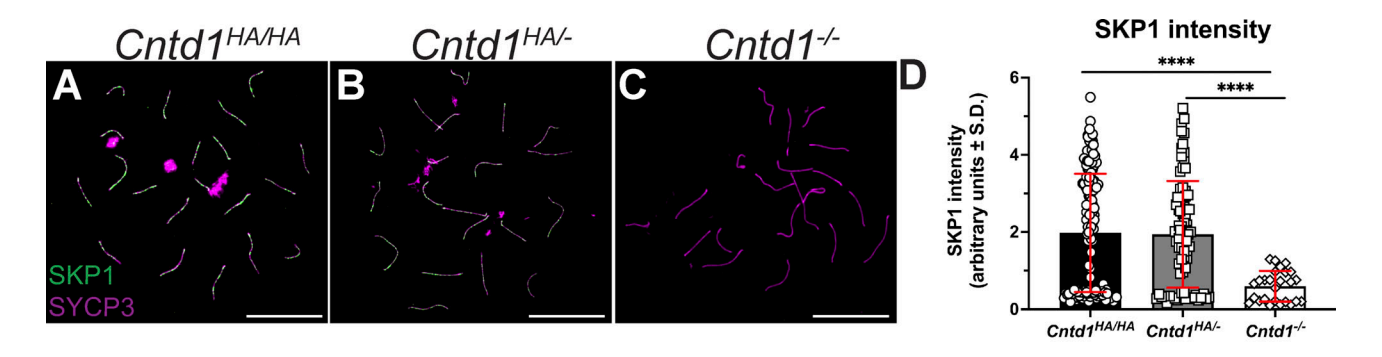
60%; Cntd1^{-/-}: 13%), and diplonema (Cntd1^{HA/HA}: 21%; Cntd1^{HA/-}: 28%; Cntd1^{-/-}: 79%). Leptonema- and zygonema-staged oocyte representative images were obtained from 16.5 and 17.5 dpc fetal ovaries. For 17.5 dpc, $n \ge 2$, and for 18.5 dpc, $n \ge 4$ biological replicates were used per genotype for progression analysis. Error bars denote the standard deviation. White scale bars are equal to 20 µm. A chi-square test was used to assess significance (****P < 0.0001).

(Bolcun-Filas et al., 2014; Martínez-Marchal et al., 2020; Rinaldi et al., 2017). Thus, we asked whether the early loss of oocytes in Cntd1^{-/-} ovaries could be reversed by the loss of either CHK1 or CHK2, placing CNTD1 within these checkpoint pathways and further explaining the mechanism underlying the loss of follicles in Cntd1^{-/-} ovaries.

Due to the embryonic lethality associated with Chk1 elimination, we utilized a pharmacological approach using a previously published in vitro culture system on PND5 ovaries treated with either DMSO or a CHK1 inhibitor (CHK1i) rabusertib (LY2603618) to determine whether oocyte loss in Cntd1^{-/-} was CHK1-dependent (King et al., 2014; Liu et al., 2000; Martínez-Marchal et al., 2020) (Fig. 8 A). We exposed one ovary per fetus to DMSO and the other to CHK1i. After incubation, we quantified oocytes positive for DDX4, a germ cell marker in oocytes from both ovaries, as previously published (Martínez-Marchal et al., 2020). CHK1i exposure resulted in no change in the average number (n) of oocytes in Cntd1HA/HA ovaries exposed to DMSO

(n = 818 oocytes) or CHK1i (n = 998 oocytes) (Fig. 8, B, C, and H;)and Table S2), nor did those from $Cntdl^{HA/-}$ ovaries exposed to DMSO (n = 772 oocytes) or CHK1i (n = 510 oocytes) (Fig. 8, D, E, and H; and Table S2). Treatment of Cntd1-/- ovaries with CHK1i (n = 281 oocytes) produced a statistically significant change in the number of oocytes compared to those treated with DMSO (n = 77oocytes) and showed that Cntd1-/- ovaries are being lost in a CHK1-dependent manner (Fig. 8, F-H and Table S2).

Due to the aberrant repair in *Cntd1* mutant oocytes, we next determined whether CHK2 was being activated (Figs. 4 and 5). To do so, we bred our Cntd1 mutant line with Chk2 mutants to generate double homozygous mutant animals (Chk2^{-/-};Cntd1^{-/-}) and associated control genotypes. We analyzed follicle composition from females at PND28 because primordial follicle loss in the Cntd1 homozygous mutant females is prevalent at this age (Fig. 3 L and Fig. 9, A-J). If CHK2 is essential for oocyte elimination in the same pathway as CNTD1, we would expect to see a rescue of primordial follicles in the absence of CNTD1, if not all follicle types.



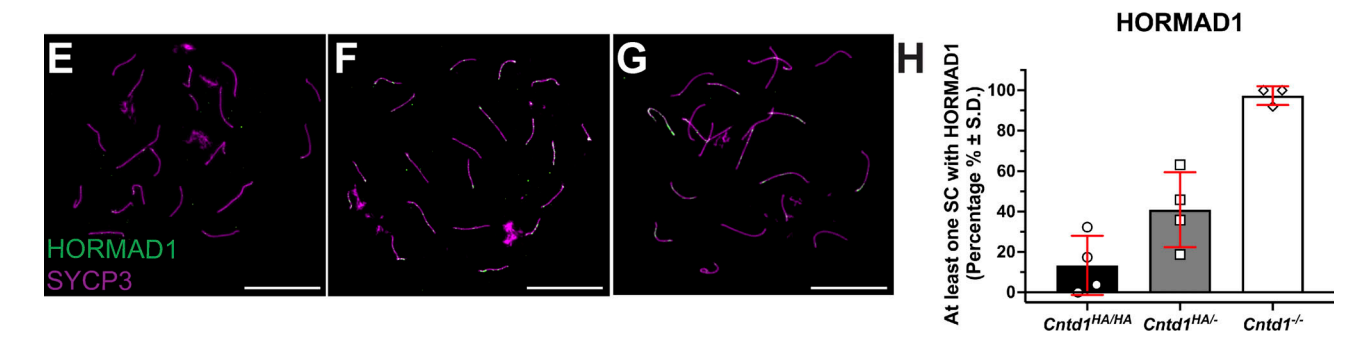


Figure 7. HORMAD1 and SKP1 are aberrant in Cntd1^{-/-} oocytes. (A-G) Localization of SKP1 (A-C) and HORMAD1 in green (E-G) with SYCP3 (magenta) on chromosome spreads from Cntd1^{HA/HA}, Cntd1^{HA/-}, and Cntd1^{-/-} oocytes from 18.5 dpc ovaries at pachynema. (D) Quantification of the intensity of SKP1 was normalized to DAPI in pachytene-staged cells (mean intensity in arbitrary units ± SD), Cntd1^{HA/HA} (SKP1, n = 142 nuclei; 2.0 ± 1.5), Cntd1^{HA/-} (SKP1, n = 81 nuclei; 1.9 ± 1.4), $Cntd1^{-/-}$ (SKP1, n = 26 nuclei; 0.60 ± 0.40). Statistical analysis: $Cntd1^{HA/HA}$ and $Cntd1^{HA/-}$: P = 0.5569, $Cntd1^{HA/HA}$ and $Cntd1^{HA/-}$: P < 0.0001, $Cntd1^{HA/-}$. and Cntd1^{-/-}: P < 0.0001. (H) Quantification of oocytes from 18.5 dpc ovaries for pachytene-staged nuclei with at least one SC with HORMAD1 present (Materials and methods). For the HORMAD1 analysis: (mean percentage ± SD) Cntd1^{HA/HA} (HORMAD1 n = 132 nuclei; 13 ± 15), Cntd1^{HA/-} (HORMAD1 n = 149 nuclei; 41 ± 19), and Cntd1^{-/-} (HORMAD1 n = 40 nuclei; 97 ± 4.6). n ≥ 3 fetuses were used for each analysis. Mean and standard deviation lines are in red. White scale bars are equal to 20 μm. A Mann-Whitney test was utilized to test for statistical significance. P values are as follows: *P < 0.05, **P < 0.001, ***P < 0.0002, ****P < 0.0001.

Wood et al. Journal of Cell Biology CNTD1 is critical for meiosis in female mice



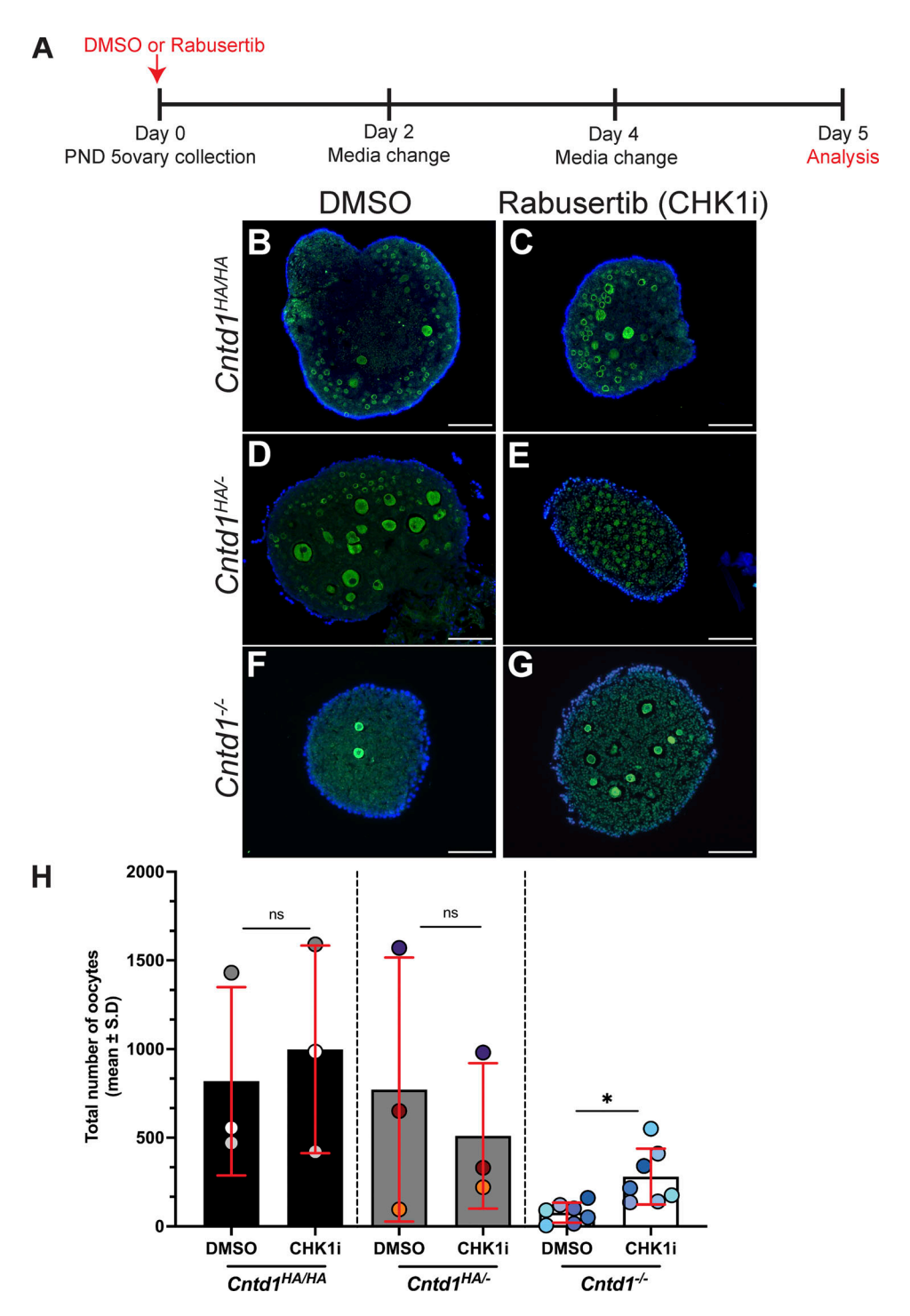


Figure 8. *Chk1* inhibition in vitro does not rescue oocyte loss in PND5 *Cntd1*^{-/-} ovaries. (A) Culture system outline with rabusertib for PND5 ovaries from Martínez-Marchal et al. (2020). (B-G) Histological sections (5 μ m) of PND5 immunostained ovaries with DDX4 (green) and DAPI (blue) of $Cntd1^{HA/HA}$, $Cntd1^{HA/-}$, and $Cntd1^{-/-}$. (H) Quantification (mean oocyte number ± SD) of all DDX4-positive oocytes from $Cntd1^{HA/HA}$ (DMSO: 818 ± 531; CHK1i: 998 ± 585), $Cntd1^{HA/-}$ (DMSO: 772 ± 745; CHK1i: 510 ± 411), and $Cntd1^{-/-}$ (DMSO: 77 ± 57; CHK1i: 281 ± 158). DMSO- and CHK1i-treated ovaries (statistical analysis—DMSO versus CHK1i: $Cntd1^{HA/HA}$: P = 0.3245, $Cntd1^{HA/-}$: P = 0.3362, and $Cntd1^{-/-}$: P = 0.0222). Oocytes from $Cntd1^{HA/-}$ ovaries were quantified. The scale bar is equal to 100 μ m. Mean and standard deviation lines are in red. Significance was determined using a paired $Cntd1^{-/-}$ test. P values are as follows: *P < 0.05, **P < 0.001, ***P < 0.0002, ****P < 0.0001.

Primordial follicles were significantly reduced in $Chk2^{+/+}$; $Cntd1^{-/-}$ females compared with $Chk2^{+/+}$; $Cntd1^{+/+}$ females (Fig. 9 K and Table S2), consistent with the drastic follicle loss we observed in $Cntd1^{-/-}$ ovaries (Fig. 3). Consistent with prior reports of $Chk2^{-/-}$ ovaries, primordial and primary follicle populations

were significantly increased in $Chk2^{-/-}$; $Cntdl^{+/+}$ compared with $Chk2^{+/+}$; $Cntdl^{+/+}$ (Fig. 9, K and L; and Table S2) (Bolcun-Filas et al., 2014). If Cntdl mutant oocytes were being lost through activation of the CHK2 kinase, we expected to see an increase in the number of primordial follicles in $Chk2^{-/-}$; $Cntdl^{-/-}$ compared with



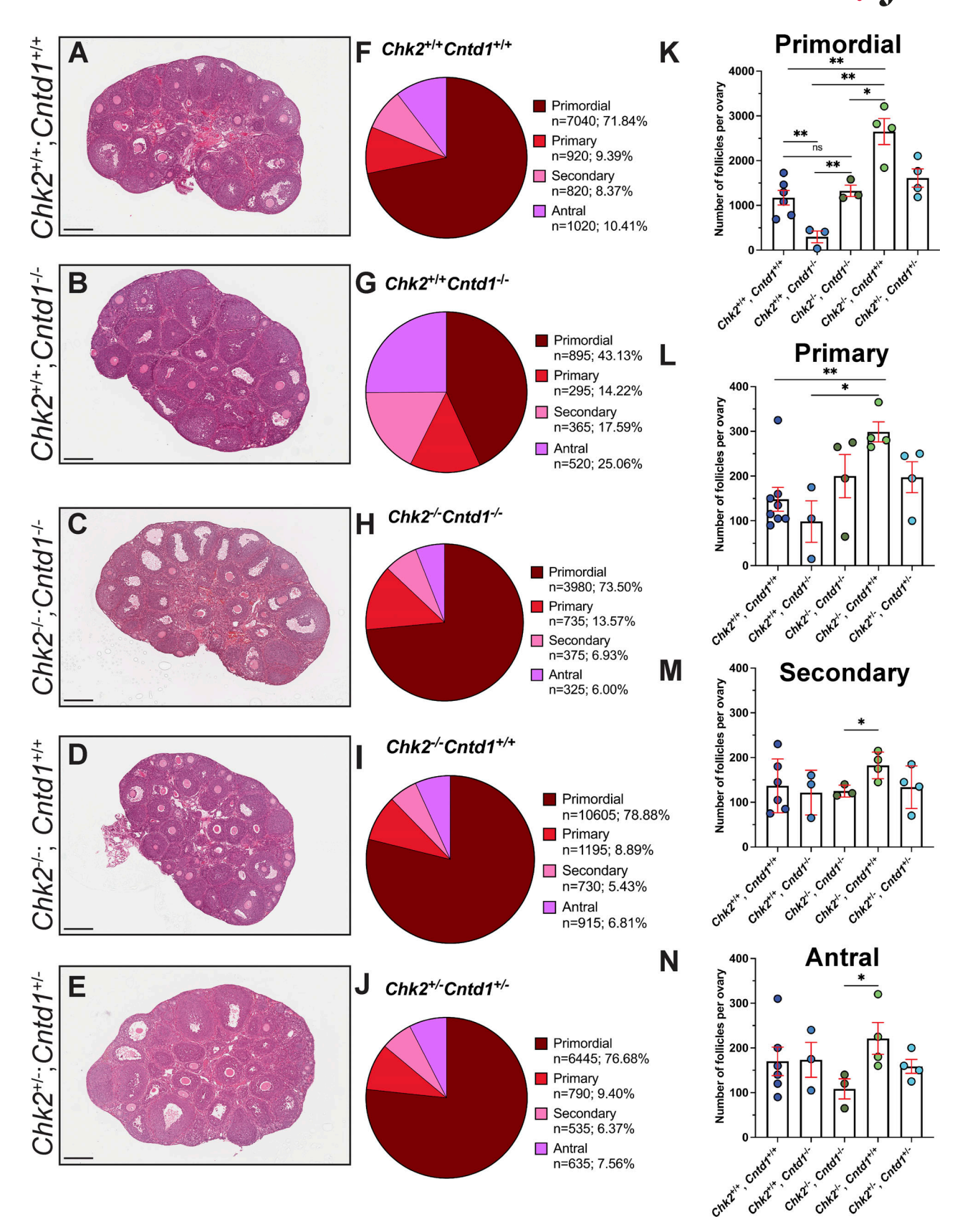


Figure 9. **Ablation of** *Chk2* **results in primordial follicle rescue in** *Cntd1*^{-/-} **oocytes. (A–E)** Histological sections of ovaries from PND28 female mice. Paraffin-embedded tissues were sectioned at 5 μm and stained with hematoxylin and eosin. Scale bars are equal to 200 μm. **(F–J)** Composition of primordial (dark red), primary (red), secondary (light pink), and antral (purple) follicle populations for each genotype visualized as a percent value for (F) *Chk2*^{+/+};*Cntd1*^{+/+}, (G) *Chk2*^{+/+};*Cntd1*^{-/-}, (H) *Chk2*^{-/-}; *Cntd1*^{-/-}, (I) *Cntd1*^{-/-}; *Chk2*^{+/+};*Cntd1*^{+/+}, and (J) *Chk2*^{+/-};*Cntd1*^{+/-} ovaries. *N* represents the total number of follicles for the



respective follicle type with a percent value, calculated as the total number of follicle types divided by the total number of follicles for all follicle types. (K-N) Quantification (average follicle number ± SD) of primordial (K) (Chk2+/+; Cntd1+/+: 1,173 ± 400, (G) Chk2+/+; Cntd1-/-: 298 ± 229, Chk2-/-; Cntd1-/-: 1,327 ± 221, Chk2^{-/-};Cntd1^{+/+}: 2,651 ± 580, and Chk2^{+/-};Cntd1^{+/-}: 1,611 ± 407), primary (L) (Chk2^{+/+};Cntd1^{+/+}: 148 ± 75, Chk2^{+/+};Cntd1^{-/-}: 98 ± 80, Chk2^{-/-}; Cntd1^{-/-}: 200 ± 97 , $Chk2^{-/-}$; $Cntd1^{+/+}$: 299 ± 45 , and $Chk2^{+/-}$; $Cntd1^{+/-}$: 198 ± 70), secondary (M) ($Chk2^{+/+}$; $Cntd1^{-/+}$: 137 ± 60 , $Chk2^{+/+}$; $Cntd1^{-/-}$: 122 ± 50 , $Chk2^{-/-}$; $Cntd1^{-/-}$: 125 + 70), Secondary (M) ($Shk2^{+/+}$); $Shk2^{-/-}$; $Shk2^{-/$ \pm 13, $Chk2^{-/-}$; $Cntd1^{+/+}$: 183 \pm 30, and $Chk2^{+/-}$; $Cntd1^{+/-}$: 134 \pm 48), and antral follicles (N) ($Chk2^{+/+}$; $Cntd1^{+/+}$: 170 \pm 78, $Chk2^{+/+}$; $Cntd1^{-/-}$: 173 \pm 68, $Chk2^{-/-}$; $Cntd1^{-/-}$: 174 \pm 68, $Chk2^{-/-}$; $Cntd1^{-/-}$: 175 \pm 78, $Chk2^{+/+}$; $Cntd1^{-/-}$: 176 \pm 78, $Chk2^{-/-}$; $Cntd1^{-/-}$: 177 \pm 68, $Chk2^{-/-}$; $Cntd1^{-/-}$: 178 \pm 68, $Chk2^{-/-}$; $Cntd1^{-/-}$: 179 \pm 78, $Chk2^{-/-}$; $Cntd1^{-/-}$: 179 \pm 79, $Chk2^{-/-}$; $Cntd1^{-/-}$; 108 ± 39 , $Chk2^{-/-}$; $Cntd1^{+/+}$: 221 ± 71 , and $Chk2^{+/-}$; $Cntd1^{+/-}$: 159 ± 31). Statistical analysis—primordial follicles: $Chk2^{+/+}$; $Cntd1^{+/+}$ and $Chk2^{+/+}$; $Cntd1^{-/-}$: P = 0.0048, $Chk2^{+/+}$; $Cntd1^{+/+}$ and $Chk2^{+/-}$; $Cntd1^{+/-}$: P = 0.1408, $Chk2^{+/+}$; $Cntd1^{+/+}$ and $Chk2^{-/-}$; $Cntd1^{+/+}$: P = 0.0071, $Chk2^{+/+}$; $Cntd1^{+/+}$ and $Chk2^{-/-}$; $Cntd1^{-/-}$: P = 0.4848, $Chk2^{+/+}$; $Cntd1^{-/-}$: P = 0.4848, $Chk2^{-/-}$; $Cntd1^{-/-}$: $Cntd1^{-/-}$: CntCntd1^{-/-} and Chk2^{-/-};Cntd1^{+/+}: P = 0.0016, Chk2^{+/+};Cntd1^{-/-} and Chk2^{-/-}; Cntd1^{-/-}: P = 0.005, Chk2^{-/-};Cntd1^{+/+} and Chk2^{-/-}; Cntd1^{-/-}: P = 0.0136. Statistical analysis—primary follicles: $Chk2^{+/+}$; $Cntd1^{+/+}$ and $Chk2^{+/+}$; $Cntd1^{+/-}$: P = 0.4121, $Chk2^{+/+}$; $Cntd1^{+/+}$ and $Chk2^{+/-}$; $Cntd1^{+/-}$: P = 0.2293, $Chk2^{+/+}$; $Cntd1^{+/-}$ and $Chk2^{-/-}$; $Cntd1^{+/+}$: P = 0.0018, $Chk2^{+/+}$; $Cntd1^{-/-}$ and $Chk2^{-/-}$; $Cntd1^{-/-}$: P = 0.3917, $Chk2^{+/+}$; $Cntd1^{-/-}$ and $Chk2^{-/-}$; $Cntd1^{-/-}$: P = 0.0311, $Chk2^{+/+}$; $Cntd1^{-/-}$ and $Chk2^{-/-}$; CP = 0.1909, $Chk2^{-/-}$; $Cntd1^{+/+}$ and $Chk2^{-/-}$; $Cntd1^{-/-}$: P = 0.1339. Statistical analysis—secondary follicles: $Chk2^{+/+}$; $Cntd1^{+/+}$ and $Chk2^{+/+}$; $Cntd1^{-/-}$: P = 0.7093, $Chk2^{+/+}$; $Cntd1^{+/+}$ and $Chk2^{+/-}$; $Cntd1^{+/-}$: P = 0.9343, $Chk2^{+/+}$; $Cntd1^{+/+}$ and $Chk2^{-/-}$; $Cntd1^{+/+}$: P = 0.1515, $Chk2^{+/+}$; $Cntd1^{+/+}$ and $Chk2^{-/-}$; $Cntd1^{-/-}$: P = 0.6667, $Chk2^{+/+}$; $Cntd1^{-/-}$: P = 0.6667, $Chk2^{-/-}$; $Cntd1^{-/-}$: $Cntd1^{ Cntd1^{-/-}$ and $Chk2^{-/-}$; $Cntd1^{+/+}$: P = 0.1564, $Chk2^{+/+}$; $Cntd1^{-/-}$ and $Chk2^{-/-}$; $Cntd1^{-/-}$: P = 0.9203, $Chk2^{-/-}$; $Cntd1^{+/+}$ and $Chk2^{-/-}$; $Cntd1^{-/-}$: P = 0.0234. Statistical analysis—antral follicles: $Chk2^{+/+}$; $Cntd1^{+/-}$ and $Chk2^{+/+}$; $Cntd1^{-/-}$: P = 0.9499, $Chk2^{+/+}$; $Cntd1^{+/-}$ and $Chk2^{+/-}$; $Cntd1^{+/-}$: P = 0.7602, $Chk2^{+/+}$; $Cntd1^{+/-}$ and $Chk2^{-/-}$; $Cntd1^{+/-}$ and $Chk2^{-/-}$ and $Chk2^{-/-}$ and $Chk2^{-/-}$ and $Chk2^{-/-}$ and $Chk2^{-/-}$ $Cntd1^{+/+}$: P = 0.3188, $Chk2^{+/+}$; $Cntd1^{+/+}$ and $Chk2^{-/-}$; $Cntd1^{-/-}$: P = 0.1577, $Chk2^{+/+}$; $Cntd1^{-/-}$ and $Chk2^{-/-}$; $Cntd1^{-/-}$: P = 0.4092, $Chk2^{+/+}$; $Cntd1^{-/-}$ and $Chk2^{-/-}$; $Cntd1^{-/-}$: $Cntd1^{-/-}$ and $Chk2^{-/-}$; $Cntd1^{-/-}$ and $Chk2^{-/-}$; $Cntd1^{-/-}$: $Cntd1^{-/-}$ and $Chk2^{-/-}$; $Cntd1^{-/-}$ and $Chk2^{-/-}$ P = 0.2388, Chk2^{-/-};Cntd1^{+/+} and Chk2^{-/-}; Cntd1^{-/-}: P = 0.0462. Follicles from n ≥ 3 ovaries were quantified per genotype. Mean and standard deviation lines are in red. Significance between genotypes of interest was determined using Welch's t test. P values are as follows: *P < 0.05, **P < 0.001, ***P < 0.0002, ****P < 0.0001.

Chk2+/+; Cntd1-/-. Indeed, when we compared the number of primordial follicles between Chk2^{-/-}; Cntd1^{-/-} and Chk2^{+/+}; Cntd1^{-/-}, we found that genetically ablating Chk2 in the absence of Cntd1 leads to a rescue in the number of primordial follicles (Fig. 9, G, H, and K; and Table S2). We also observed a statistical increase in the population of primordial follicles in Chk2^{-/-}; Cntd1+/+ individuals compared with Chk2-/-;Cntd1-/- (Fig. 9 K and Table S2). Moreover, the importance of CHK2 in eliminating Cntd1 mutant oocytes was reinforced by the lack of statistical significance between Chk2+/+;Cntd1+/+ and Chk2-/-;Cntd1-/- in the average number of primordial follicles, indicating that statistically full rescue was achieved (Fig. 9 K and Table S2). A significant increase in secondary and antral follicles was observed in Chk2-/-; Cntd1+/+ compared with Chk2-/-; Cntd1-/- ovaries (Fig. 9, M and N; and Table S2). Together, these data demonstrate that Cntd1-/- oocytes are being lost through CHK1and CHK2-dependent pathways.

Discussion

Defects in CO regulation, synapsis, and quality control checkpoints, which arise disproportionately in meiosis I, account for the dimorphism in aneuploidy rates between the sexes (Hassold and Hunt, 2001; Hassold et al., 2021; Lenzi et al., 2005; Nagaoka et al., 2012). Given these data, studies unraveling the molecular dynamics of CO regulation in mammalian oocytes are crucial. However, technical challenges associated with isolating oocytes at early developmental time points have hindered such studies in females. The current study was aimed at understanding the function of one key regulator of CO formation, CNTD1, in mammalian oogenesis. We sought to understand the role of CNTD1 in the regulation of CO designation and cell cycle regulation compared with analogous events in males to better understand the high rate of CO failure in oocytes compared with spermatocytes.

Cyclin-independent form of CNTD1 is present in both mammalian spermatocytes and oocytes

The discovery that CNTD1 exists only as a smaller-than-predicted form in mouse testes was unexpected, but suggests a unique cyclin-independent function of CNTD1 that is distinct from its worm ortholog, COSA-1 (Gray et al., 2020) since the smaller size of mouse CNTD1 is predicted to lack an N-terminal cyclin homology domain that is essential for interaction with CDK2. Our studies confirm that this truncated isoform is the only detectable form in both mouse oocytes and spermatocytes and mammals, including humans. Evidence includes the following: (1) an antibody against HA (in Cntd1-HA-expressing mice) reveals the presence of a single band for CNTD1 in mouse testis and ovary that migrates more quickly than the predicted full-length CNTD1, thus indicating a smaller sized protein (Fig. 2); (2) our observation of the predominance of smallerthan-predicted CNTD1 in mouse testis was supported by studies of Bondarieva et al., who show a single CNTD1 band that is indicative of this size using a custom antibody against CNTD1 (Fig. 2) (Bondarieva et al., 2020); (3) a similarly short form of CNTD1 is also observed in spermatocytes from several mammalian species (Fig. S2 D); (4) immunoprecipitation of CNTD1 from mouse spermatocytes reveals no interactions with any known CDK, both by western blotting and by mass spectrometry (Bondarieva et al., 2020; Gray et al., 2020); and (5) previous yeast two-hybrid analysis demonstrates that CNTD1SF (an isoform lacking an N-terminal cyclin homology domain) fails to interact with any CDK, while full-length CNTD1 can interact with several CDKs (Gray et al., 2020). Taken together, this in vivo evidence suggests that mammalian CNTD1 is present as a short form that lacks a key cyclin homology domain, and this form may be generated by a later translational start site at Met86 (Gray et al., 2020), a possibility that is currently under investigation using in vitro biochemical methods. Although our studies indicate that only one short form of CNTD1 exists in mammalian germ cells, we acknowledge the possibility that a cyclin-like form of CNTD1 may be present at levels that are below the limits of detection.

CNTD1 is essential for the formation of class I COs and synapsis between homologous chromosomes in mammalian oocytes

Repair of all DSBs and full synapsis of homologous chromosomes are essential in oocytes during prophase I. In males, defects in



either of these processes are sufficient to robustly induce quality control checkpoints leading to loss of spermatocytes, while in females, oocytes appear to be tolerant to such errors (Bolcun-Filas et al., 2014; Ravindranathan et al., 2022; Rinaldi et al., 2020). Our findings show that $CntdI^{-/-}$ oocytes have defective DSB repair, marked by a complete loss of class I COs (Fig. 1). The persistence of 1–2 residual bivalent chromosomes in diakinesis oocytes from $CntdI^{-/-}$ animals is also observed in other CO mutants (Prr19, Rnf212b, Mlh1, and Mlh3) and suggests an intact class II CO pathway catalyzed by the activity of the structure-specific endonuclease MUS81-EME1 (Bondarieva et al., 2020; Condezo et al., 2024; Holloway et al., 2008; Ito et al., 2023, Preprint; Kan et al., 2008; Woods et al., 1999). Taken together, our data indicate that CNTD1 functions specifically in the class I CO pathway and is essential for proper CO site selection.

Pachytene-staged $Cntdl^{-/-}$ oocytes from 18.5 dpc ovaries show delayed/aberrant DSB repair (RAD51 and γ H2A.X), although the persistence of RAD51 foci (Fig. 4) falls below the published threshold of DSB tolerance (>10 DSBs), and reduced γ H2A.X intensity (Fig. 5) could indicate DSB repair is not occurring efficiently or oocytes are lost before pachynema (Rinaldi et al., 2017). At 17.5 dpc, pachytene-staged oocytes display no difference in γ H2A.X intensity and RAD51 foci, and could indicate that oocytes are lost prior to this time point, as cohorts of oocytes progress through prophase I in an asynchronous manner (Menke et al., 2003). These findings suggest that CNTD1 impacts the timely repair of DSBs, although these deficiencies are likely not sufficient to result in the induction of the DSB checkpoint.

Synapsis between homologous chromosomes is critical for the timely and accurate repair of DSBs in meiotic prophase I. Defects in establishing and maintaining synapsis can result in the activation of the pachytene checkpoint, resulting in the death of oocytes before dictyate arrest (Huang and Roig, 2023; Wang and Pepling, 2021). At 18.5 dpc, we observed decreased pachytene oocytes and a concomitant increase in diplotene oocytes in *Cntd1*^{-/-} females, coupled with retention of HORMAD1, and reduced SKP1 intensity in pachytene-staged oocytes (Figs. 6 and 7; and Fig. S4, E-L). Both the disrupted progression through prophase I and the altered SKP1 and HORMAD1 localization are unique in Cntd1^{-/-} oocytes, and not observed in other CO regulator mutants such as Heilo, Rnf212, Rnf212b, Prr19, or Cntd1-/spermatocytes. However, accelerated prophase I progression was reported in Skp1cKO oocytes and Chk2 mutant oocytes (Guan et al., 2022; Martínez-Marchal et al., 2020), strongly supporting our link between CNTD1 dysfunction and loss of SKP1. SKP1 is a core component of the SCF complex, is essential for cell cycle progression and synapsis in mammalian meiocytes, and has been reported to have an independent function as part of the SC in C. elegans (Blundon et al., 2024; Guan et al., 2020, 2022). Indeed, SkplcKO mammalian meiocytes phenocopy the defect in synapsis we observe in Cntdl mutant oocytes (Guan et al., 2020, 2022). Our previous work has reported that CNTD1 in mouse spermatocytes complexes with CDC34, an E2 ubiquitinconjugating enzyme that is known to function with the SCF complex (Gray et al., 2020). From these reports, we conclude that CNTD1 in oocytes may have an independent function

outside of CO formation to maintain synapsis and/or remove HORMAD1 in the same pathway as SKP1 during meiotic prophase I.

Loss of *Cntd1* results in a primary ovarian insufficiency phenotype, which is rescued by genetic ablation of *Chk2* and pharmacological inhibition of CHK1

At the end of prophase I, oocytes arrest in dictyate and become enclosed in primordial follicles that steadily develop into successive follicular stages, culminating in ovulation in response to pituitary gonadotropins (Hassold et al., 2021; Morelli and Cohen, 2005; Tingen et al., 2009a; Wang and Pepling, 2021). The majority of primordial follicles are lost soon after birth in a normal process called atresia (Baker, 1963; Tingen et al., 2009a, 2009b). Excessive loss of oocytes and follicles can lead to primordial ovarian insufficiency (POI), a condition causing infertility before the age of 40 (Guo et al., 2017; Huang et al., 2021; Ke et al., 2023; Veitia, 2020). Previous studies of a number of female meiotic mouse mutants reveal a conserved mechanism whereby defective DSB repair and synapsis trigger one of two quality control checkpoint kinases, CHK1 and CHK2, and all such mutants display POI-like phenotypes (Bolcun-Filas et al., 2014; Di Giacomo et al., 2005; Rinaldi et al., 2017, 2020).

Studies reported herein demonstrate that loss of CNTD1 results in the loss of oocytes starting shortly after birth and this loss is temporally distinct from early and late CO regulators (Figs. 3 and S5). Briefly, early prophase I mutants have defects from zygonema onward, resulting in rapid oocyte loss before birth, and have necrotic-appearing ovaries devoid of follicles by adulthood (Edelmann et al., 1999; Kneitz et al., 2000). Late prophase I mutants have similar meiotic phenotypes to Cntdl-/females, showing loss of chiasmata at diakinesis, but no detailed report of alterations to the follicle populations (Kan et al., 2008; Lipkin et al., 2002; Woods et al., 1999). This difference between prophase I function and follicular phenotypic consequence may reflect the additional roles of CNTD1 in meiotic cell cycle regulation and/or checkpoint signaling.

The checkpoint kinases Chk1 and Chk2 are the predominant regulators in oocyte quality control (Huang and Roig, 2023; Martínez-Marchal et al., 2020). In the context of meiosis, these kinases are triggered by defects in DNA damage repair and failure of synapsis and subsequent signaling by upstream effectors (Di Giacomo et al., 2005; Martínez-Marchal et al., 2020; Rinaldi et al., 2017, 2020). Mouse mutants that bear mutations in DSB repair (Spoll and Dmcl) or synapsis (Tripl3) can be rescued by the concurrent loss of Chk2, highlighting its role in eliminating defective oocytes (Bolcun-Filas et al., 2014; Rinaldi et al., 2017). Chk2^{-/-}; Cntd1^{-/-} ovaries show an increase in the number of primordial follicles in PND28 animals relative to Chk2+/+; Cntd1-/- females (Fig. 9 K), and follicle numbers in Cntd1-/- are rescued by in vitro inhibition of CHK1 activity (Fig. 8 H). Together, these data lead us to conclude that in addition to its role in the regulation of class I CO formation, Cntd1 plays a novel role in maintaining oocyte quality up until the pachytene checkpoint, through the recruitment of SKP1 and removal of HORMAD1.

Taken together, the data presented herein reveal two distinct functions of CNTD1 in prophase I in mammalian oocytes. First,



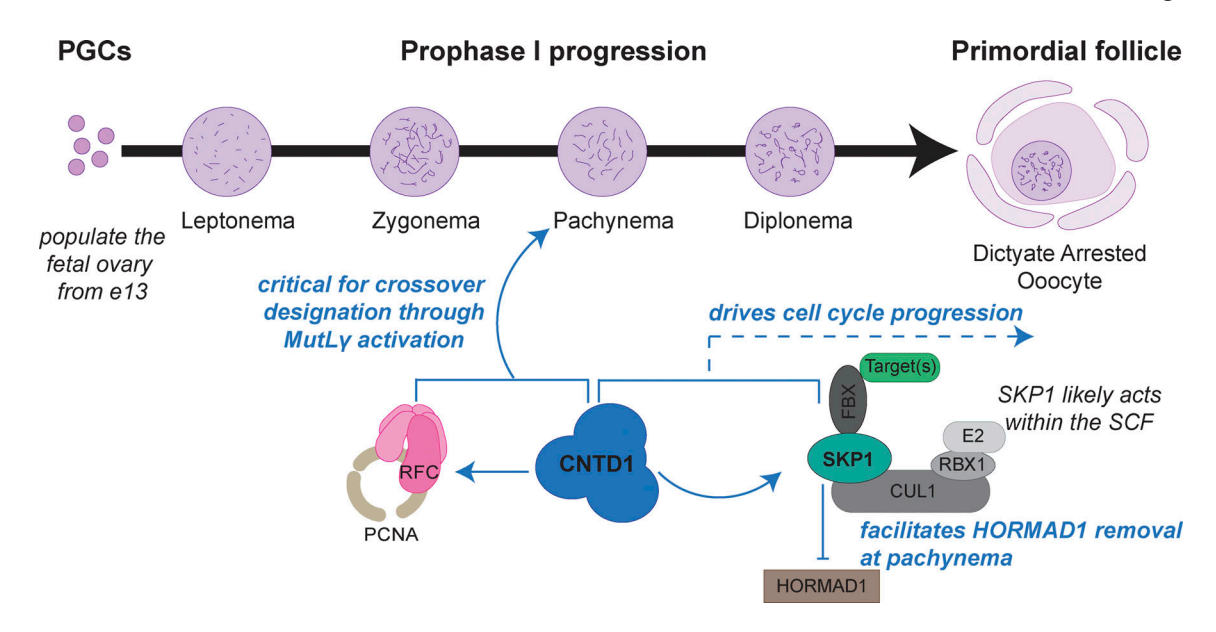


Figure 10. **Dual role of CNTD1 during prophase I in promoting CO formation and progression in mouse meiosis.** The proposed functions of CNTD1 are shown in blue. Our previous studies demonstrated interactions between CNTD1 and RFC, and between CNTD1 and multiple components of the SCF complex (Gray et al., 2020). In the current study, our phenotypic characterization of *Cntd1*^{-/-} females shows that CNTD1 is essential for establishing MutLy-dependent COs in pachynema. Thus, together with our previous proteomics data, we propose that this role of CNTD1 occurs through putative interactions with RFC and its partner, PCNA. Our previous proteomics data also revealed interactions with multiple components of SCF, which confer its specificity for its targets. Studies of the loss of CNTD1 in both male and female meiosis presented herein indicate that the interaction of CNTD1 with SCF facilitates cell cycle progression, leading to altered progression through prophase I. Additionally, or as part of this mechanism, this current study reveals that the loss of CNTD1 results in reduced SKP1 and a concomitant retention of HORMAD1. We hypothesize that the altered prophase I progression we observe results from CNTD1-induced retention of HORMAD1 through a SKP1 function that may or may not be dependent on SCF. This hypothesis is supported by studies by other groups demonstrating that SKP1 removes HORMAD1 during pachynema (Guan et al., 2022). We further propose that CNTD1 influences the action of SKP1/SCF on other targets that may function to regulate cell cycle progression in both male and female meiosis. RFC, replication factor C.

CNTD1 ensures that class I COs are established, leading to accurate segregation of chromosomes at the first meiotic division, likely through its interaction with RFC (Fig. 10). Second, CNTD1 plays a unique role in regulating cell cycle progression and activation of the oocyte quality control checkpoints through interactions with SCF complex components at the SC, as demonstrated by the follicle loss phenotype, which is distinct from other early and late pro-CO factors (Figs. 3, 9, and 10). Future studies focusing on elucidating the dual function of CNTD1 in facilitating CO formation and then signaling to advance the cell cycle, particularly in female meiosis, are likely to yield critical information that elucidates why mammalian oogenesis is so error-prone.

Materials and methods

Mouse strains

All mouse strains were maintained on a C57BL/6J background. CntdI^{HA} and CntdI^{-/-} mouse strains were used as reported previously (Gray et al., 2020). Briefly, both mouse lines were generated by the Cornell Stem Cell and Transgenic Core Facility using the CRISPR/Cas9 technology. The CntdI^{HA} line was generated by inserting a FLAG-HA epitope tag at the 3' end of the endogenous CntdI locus using a CntdI-specific sequence (5'-GCC GCTTCCTCTAACACGTG-3') into the pX330 plasmid. This region was amplified to integrate a T7 promoter and subsequently used with Ambion MEGAshortscript T7 Transcription Kit (AM1354).

The gRNA and donor template were used in combination with CRISPR/Cas9 technology to generate C57BL/6J x FVP F1 zygotes. Founders containing the Flag-HA allele in-frame were backcrossed for at least four generations with C57BL/6J animals prior to experiments. The mutant allele of Cntd1 was generated by inducing a DSB with the corresponding gRNA in the endogenous locus of Cntd1, and founders containing a frameshift mutation were sequence-verified and found to have a 324-bp insertion on chromosome 12, which resulted in the disruption of the Cntd1 open reading frame. The Cntd1-Flag-HA mice were generated by breeding Cntd1-Flaq-HA allele-containing and Cntd1 mutant allele-containing animals together to generate mice with an allele of Flag-HA and a mutant allele. Validation of these mice confirmed their appropriate expression of a modified Cntd1-Flag-HA allele or no Cntdl expression, respectively. The presence of the Cntd1-Flag-HA allele (\sim 327 bp) or the Cntd1 mutant allele (\sim 273 bp) was achieved by PCR amplification using the Cntdl_HA_Fwd and Cntd1_HA_Rev primers and the following thermal cycling conditions: initial denaturation at 98°C for 2 min, and 35X of the following conditions: denaturation at 98°C for 30 s, annealing at 62°C for 30 s, extension at 72°C for 1 min, and a final extension at 72°C for 2 min. The reaction was held at 4°C until subsequent analysis with gel electrophoresis.

All mice were maintained under strictly defined conditions of constant temperature and light:day cycles, with food and water ad libitum. Animal handling and procedures were performed following approval by the Cornell Institutional Animal Care and



Use Committee, under protocol 2004-0063. All experimental animals were genotyped from ear snips collected and processed with 0.05 M NaOH and 1 M Tris-HCl, pH 7.2. The $\it Chk2$ mutant mice were obtained as a generous gift from Dr. John Schimenti (Cornell University, Ithaca. NY, USA). The Chk2; Cntd1 compounds were generated initially by mating Chk2+/- and Cntd1+/individuals. Offspring were genotyped, and individuals that were *Chk*2^{+/-}; *Cntd*1^{+/-} were used for both experimental matings and maintenance of the line. The thermal cycling conditions are as follows for the detection of both the *Chk*2 wild-type (\sim 170 bp) and Chk2 mutant alleles (~200 bp): initial denaturation at 95°C for 5 min, and 36X of the following conditions: denaturation at 95°C for 30 s, annealing at 60°C for 30 s, extension at 72°C for 30 s, and a final extension at 72°C for 5 min. The reaction was held at 4°C until subsequent analysis with gel electrophoresis. The concurrent Cntdl genotype of these mutants was determined with primers CNTD1_mut_F and CNTD1_mut_R and the following thermal cycling conditions to detect the wild-type (~167 bp) or mutant (~491 bp) alleles: initial denaturation at 98°C for 2 min, and 35X of the following conditions: denaturation at 98°C for 30 s, annealing at 49°C for 30 s, extension at 72°C for 1 min, and a final extension at 72°C for 2 min. The reaction was held at 4°C until subsequent analysis with gel electrophoresis.

Breeding assay

Two Cntdl^{HA/HA}, Cntdl^{HA/-}, or Cntdl^{-/-} females and one Cntdl^{HA/HA} male were allowed to mate for up to 3 mo. Each trio was allowed to produce pups up to 3 mo from the pairing date. Subsequent litter numbers were recorded at weaning.

Chromosome spreading and immunofluorescence

Oocytes were isolated from 16.5 to 18.5 dpc fetal ovaries, with the day of observing the vaginal plug being 0.5 dpc. Ovaries were dissected into 1X PBS and incubated in hypotonic extraction buffer for ~20-30 min at room temperature, which comprised of Tris-HCl (pH 8.2), 50 mM sucrose, 17 mM trisodium dihydrate, 5 mM EDTA, 0.5 mM DTT, and 0.1 mM PMSF. After this incubation, the ovaries were punctured in 100 mM sucrose and added to slides containing 1% paraformaldehyde with 20% Triton X. The ovaries were allowed to fix at room temperature for 2 h in a humid chamber. After 2 h, slides were allowed to dry at room temperature. Slides were washed in a mixture of 0.4% Photo-Flo and Milli-Q H₂O once for 5 min and then allowed to dry completely. For preparation of primary antibody staining, slides were washed with 0.4% Photo-Flo in 1X PBS once for 10 min. This was followed by washing in a Triton wash comprised of 0.5% Triton and 10% antibody dilution buffer ("ADB": 3g BSA, 90 ml 1X PBS, and 20% Triton X, filter-sterilized) in 1X PBS once for 10 min followed by blocking in 10% ADB in 1X PBS for 30 min at room temperature. Slides were subsequently stained with the antibody of interest (HA 1:500, MLH1 1:50, SYCP3 [mouse] 1:500, MLH3 [guinea pig] 1:500, SYCP3 [rabbit] 1:1,000, RAD51 1:500, SYCP1 [rabbit] 1: 5,000, HORMAD1 [rabbit] 1:1,000, SKP1 [rabbit] 1:50, γH2A.X [mouse] 1:1,000) overnight at room temperature in a humid chamber. The following day, slides were washed with 0.4% Photo-Flo in 1X PBS, Triton wash, and blocked in 1X ADB as stated above. Secondary Alexa

Fluor antibodies were diluted 1:2,000 in 10X ADB, and slides were stained for 2 h at room temperature. Following secondary antibody staining, slides were washed in the dark in 0.4% Photo-Flo in 1X PBS (three 5-min washes) at room temperature, followed by a wash in 0.4% Photo-Flo in Milli-Q $\rm H_2O$ once for 5 min. Slides were allowed to dry and mounted with DAPI plus antifade (8 ng/ml) and sealed with rubber cement and imaged.

Quantitation and assessment of chromosome spread staining

For staining intensity analyses of H2A.X and SKP1, all images were taken at the same exposure time and run through a previously published script in ImageJ (Alexander et al., 2023). The ratio of 488 (GFP) divided by DAPI was taken for each cell and plotted in Prism. Normalization and descriptive statistics were recorded, and statistical significance was determined using a Mann-Whitney t test. For analysis of HORMAD1 staining, all images were taken as explained above. To declare "abnormal" HORMAD1 staining, at least one SC had a HORMAD1 signal present. Values are recorded as the percentage per fetus.

Oocyte prophase I substaging for progression analysis

The presence of a fork at the end of a long and filamentous SC as visualized by SYCP3 and no localization of SYCP1, but no bubble on the axis, were considered as zygotene-staged. Oocytes with colocalized SYCP1 and SYCP3 along the entire axis length of the SC were categorized as pachytene-staged. The presence of a bubble as marked by the presence of SYCP3, but not SYCP1, and/or a fork with no SYCP1 was considered diplotene-staged. Cells with the complete absence of SYCP1 and compact axes as marked by SYCP3, or cells with complete repulsion of compact SYCP3 axes, with no SYCP1, were also considered as diplotene-staged. Insets of the morphological characteristics explained above can be found in Fig. S3.

Ovary histology and quantification

One ovary from mice at PND1, PND14, and PND28, and 8- to 12wk-old adults were fixed in Bouin's solution or formalin for 4 h at room temperature on a nutator. Following fixation, ovaries were washed in 70% ethanol. For histological preparation, ovaries were embedded in HistoGel before being prepared in a cassette. The Cornell Histopathology Core serial-sectioned HistoGel and paraffin-embedded ovaries in 5-µm sections. Hematoxylin and eosin staining was performed as follows: three 5-min washes in Histo-Clear, followed by three 3-min washes in 95% ethanol, subsequently followed by one 5-min wash in 80% ethanol and 70% ethanol, with a final wash in 1X PBS for 10 min. The staining comprised one 30-s staining in hematoxylin followed by two washes in Milli-Q H₂O, followed by two dunks in bluing reagent and subsequent washes in Milli-Q H₂O. Slides were stained with eosin for 2 min followed by four dunks in Milli-Q H₂O. Slides were then processed through 1 dunk of 70% ethanol and 80% ethanol, and three 3-min washes in 95% ethanol, finished with three 3-min Histo-Clear washes. Slides were dried and mounted with Permount and subsequently imaged. Sections were imaged on Aperio software using an Aperio CS2 Digital Pathology Slide Scanner microscope at 40× magnification. The total number of follicles was determined by multiplying the



raw counts from every fifth section by five to correct for the sections not counted. Follicles were staged as explained previously, and follicles with oocytes without a visible nucleus were excluded from quantification to avoid double counting (Sarma et al., 2020).

Oocyte metaphase spread preparations

Spreads were prepared as previously described in Sun and Cohen (2013). Briefly, M2 collection media were made comprised of Waymouth's medium, FBS, 1% penicillin-streptomycin, and 2.5 mg/ml sodium pyruvate. A 60-mm plastic petri dish was prepared with 20 µl KSOM droplets and light mineral oil covering the droplets. Collection media and the KSOM droplets with light mineral oil were equilibrated overnight in a 37°C incubator (5% CO₂). Ovaries from unstimulated female mice aged 24-28 days were collected directly into warmed collection media. We utilized unstimulated prepubertal females due to the fragility of oocytes observed when superovulated. The ovaries were punctured using 26-gauge needles to release oocytes. Oocytes with a visible zona pellucida and cumulus cells were collected using a 150-striper tip and placed into one of the KSOM droplets. Dissociation of the cumulus cells was achieved by mouth-pipetting oocytes through the KSOM droplets until cumulus cells were gone. Oocytes in KSOM and mineral oil were incubated for ~7-8 h until the oocytes entered metaphase I. Oocytes were moved to 20 µl droplets of 1% hypotonic solution (1 g sodium citrate dissolved in 100 ml Milli-Q H₂O) for 15 min. A glass slide prepared with a China pen or hydrophobic pen in a grid formation was used. 1-2 µl of hypotonic solution was placed onto one square on the glass slide. Oocytes without the zona pellucida were transferred to the drop. Excess hypotonic solution was siphoned off to allow the oocytes to adhere to the slide. One drop of Carnoy's fixative (three parts methanol and one part glacial acetic acid) was added directly to the oocytes. The fixative was allowed to disperse, followed by another 1-2 drops of Carnoy's fixative. The slides were allowed to airdry. This was followed by Giemsa staining (48 ml Milli-Q H₂O and 2 ml Giemsa) in a Coplin jar for 3 min. The slides were washed three times for 3 min in Milli-Q H₂O. The slides were allowed to dry at room temperature, immediately followed by mounting with Permount and a coverslip. Chiasmata were imaged at 63× magnification on a Zeiss Axiophot Z1 microscope.

Immunoprecipitation of proteins from fetal mouse ovarian cell extracts

Co-immunoprecipitations were performed as reported previously with modifications (Gray et al., 2020). Approximately 40 ovaries per genotype (Cntdl^{HA/HA} or C57BL/6J) from 18.5 dpc embryos were isolated and snap-frozen on dry ice, then stored at -80°C until use. Cntdl^{HA/HA} testes were collected from 10-wk-old adults, detunicated, and snap-frozen on dry ice before storage at -80°C until use. Ovaries or testes were added to 1 ml of cold lysis buffer (50 mM Tris-HCl, pH 8.0, 0.2% NP-40, 150 mM NaCl, 5 mM EDTA, 0.1 mg/ml PMSF, Roche cOmplete EDTA-free protease inhibitor tablet) and sonicated with the following parameters: 23% amplitude for 12 s, 0.4 s on/0.2 s off, and rest on ice for ~30 s between runs. Sonicated tissues were then spun

down at 15,000 \times q for 20 min at 4°C, and the supernatant was collected. 20 µl of the lysate was removed for BCA quantification, and protein amounts were quantified based on the manufacturer's protocol. 10 µl of rabbit anti-HA-conjugated magnetic beads was added to 500 µl of lysate (250 µg total protein) and incubated overnight at 4°C. The unbound supernatant was removed from beads, and beads were washed four times for 5 min in 500 µl ice-cold wash buffer (lysis buffer with 250 mM NaCl). Beads were then resuspended in 100 µl of wash buffer and transferred to a fresh tube. Bound proteins were eluted from beads by resuspending in 30 µl elution buffer (100 mM Tris-HCl, pH 8.0, 1% SDS, and 10 mM DTT), then incubating at 65°C for 15 min. The elutant was then collected, added to 10 µl 4X Laemmli sample buffer, and boiled for 5 min at 95°C. Input gel samples were taken before the addition of HA beads: 30 µl of lysate was added to 10 µl 4X Laemmli sample buffer (Bio-Rad) and boiled at 95°C for 5 min.

SDS-PAGE and western blotting

Protein samples were separated by SDS-PAGE on gels varying in percentage from 6% to 14% and transferred to methanolactivated PVDF membranes using a Bio-Rad Mini Trans-Blot Cell. Membranes were blocked by incubating in EveryBlot Blocking Buffer at room temperature while rotating at 60 rpm for 10 min. Membranes were then incubated overnight in primary antibody (HA at 1:500 and CNTD1 [Bondarieva et al., 2020], rabbit and guinea pig at 1:2,000), CNTD1 (this study, rabbit at 1:1,000), diluted in EveryBlot Blocking Buffer at 4°C. Membranes were washed three times in 0.1% TBST and subsequently incubated with secondary antibody (1:5,000) for 1-2 h at room temperature, followed by three 0.1% TBST washes. Membranes were developed using various ECL reagents and imaged using a Bio-Rad ChemiDoc imager. Antibodies used in this study are described in the Key Resources Table (Table 1).

Preparation of animal testis for western blotting

Discarded testis tissue from cats, dogs, horses, and humans was detunicated, flash-frozen on dry ice, and stored at -80° C until use. Frozen detunicated testes were added to 1 ml of cold lysis buffer (50 mM Tris-HCl, pH 8.0, 0.2% NP-40, 150 mM NaCl, 5 mM EDTA, 0.1 mg/ml PMSF, Roche cOmplete EDTA-free protease inhibitor tablet) and sonicated with the following parameters: 23% amplitude for 12 s, 0.4 s on/0.2 s off, and rest on ice for \sim 30 s between runs. Sonicated tissues were then spun down at 15,000 × g for 20 min at 4°C, and the supernatant was collected. 20 μ l of the lysate was removed for BCA quantification, and protein amounts were quantified based on the manufacturer's protocol. The lysate was then added to 2X Laemmli sample buffer (Bio-Rad) and boiled at 95°C for 10 min. Gel samples were kept at -20° C until running on western blot.

Generation of CNTD1 antibody

Cloning of bacterial expression plasmids, purification of recombinant protein, animal immunization, and purification of antibody were performed by Proteintech (Order ID: MU052118-1). CNTD1 cDNA corresponding to 249 amino acids between Met86 and Thr334 was amplified using primers CNTD1_F and



Table 1. Key Resources Table

Reagent or resource	Source	Identifier
Antibodies		
HA (rabbit monoclonal)	Cell Signaling	3724
MLH1 (mouse)	BD Pharmingen	554073
MLH3 (guinea pig)	Custom-made	Lead contact
SYCP3 (rabbit)	Custom-made	Lead contact
SYCP3 (mouse)	Abcam	ab97672
RAD51 (rabbit)	EMD Millipore	PC130-100UL
SYCP1 (rabbit)	Abcam	ab15090
HORMAD1 (rabbit)	Proteintech	13917-1-AP
SKP1 (rabbit)	Cell Signaling	D3J4N
γH2A.X (mouse)	MilliporeSigma	JBW301
DDX4 (rabbit)	Cell Signaling	8761S
MSY2 (mouse)	Santa Cruz	sc-393840
HA-Tag rabbit mAb (magnetic bead conjugate)	Cell Signaling	11846
CNTD1 (guinea pig)	Bondarieva et al. (2020)	https://doi.org/ 10.1038/s41467 020-16885-3
CNTD1 (rabbit)	Bondarieva et al. (2020)	https://doi.org/ 10.1038/s41467 020-16885-3
CNTD1 (rabbit)	This study	S4712-2
Goat anti-rabbit IgG (H+L) secondary antibody, HRP	Thermo Fisher Scientific	31460
Alexa Fluor 488-AffiniPure F(ab')2 Fragment Goat Anti- Guinea Pig IgG (H+L)	Jackson ImmunoResearch	106-546-003
Alexa Fluor 488-AffiniPure F(ab')2 Fragment Goat Anti- Rabbit IgG	Jackson ImmunoResearch	111-546-046
Alexa Fluor 488-AffiniPure F(ab')2 Fragment Goat Anti- Mouse IgG	Jackson ImmunoResearch	115-546-071
Alexa Fluor 594–conjugated AffiniPure F(ab')2 Fragment Goat Anti- Mouse IgG	Jackson ImmunoResearch	115-586-146
Alexa Fluor 594-AffiniPure F(ab')2 Fragment Goat Anti- Rabbit IgG	Jackson ImmunoResearch	111-586-046
Alexa Fluor 647-AffiniPure F(ab')2 Fragment Goat Anti- Mouse IgG	Jackson ImmunoResearch	115-606-071
Alexa Fluor 647-AffiniPure F(ab')2 Fragment Goat Anti- Rabbit IgG	Jackson ImmunoResearch	111-606-046
Alexa Fluor 647-AffiniPure F(ab')2 Fragment Goat Anti- Guinea Pig IgG	Jackson ImmunoResearch	106-606-003
Chemicals, peptides, recombi	nant proteins, and reagents	
Western blot and immunop	orecipitations	

Table 1. Key Resources Table (Continued)

Reagent or resource	Source	Identifier
Laemmli buffer	Bio-Rad	1610747 (4X), 1610737 (2X)
Pierce BCA Protein Assay Kit	Thermo Fisher Scientific	23225
Pierce ECL western Blotting Substrate	Thermo Fisher Scientific	32106
SuperSignal West Pico PLUS Chemiluminescent Substrate	Thermo Fisher Scientific	34580
SuperSignal West Femto Maximum Sensitivity Substrate	Thermo Fisher Scientific	34096
30% acrylamide/Bis solution 37.5:1	Bio-Rad	1610158
EveryBlot Blocking Buffer	Bio-Rad	12010010
Trans-Blot Turbo 5X Transfer Buffer	Bio-Rad	10026938
TMED	Bio-Rad	161-0801
2,2,2-Trichloroethanol	Sigma-Aldrich	T54801-100 G
10X Tris/glycine/SDS buffer	Bio-Rad	1610772
Roche cOmplete EDTA- free protease inhibitor tablet	Sigma-Aldrich	1873580001
Chiasma spreads		
KSOM medium	Sigma-Aldrich	MR-101-D
Light mineral oil	MilliporeSigma	ES-005-C
Micropipettes	CooperSurgical Inc.	MXL3-150
Sodium citrate	Thermo Fisher Scientific	S279-500
Methanol	Thermo Fisher Scientific	A412-4
Acetic acid, glacial	Thermo Fisher Scientific	A38-212
Giemsa stain	Sigma-Aldrich	GS500-500L
Permount	Thermo Fisher Scientific	SP15100
EmbryoMax M2 Medium	MilliporeSigma	MR-015-D
Microscope slides	Thermo Fisher Scientific	12-544-2
Milrinone	Sigma-Aldrich	M4659-10 MG
Histology and follicle quantific	cation	
Harris hematoxylin	Thermo Fisher Scientific	NC9520196
Eosin Y solution	Thermo Fisher Scientific	E511-25
SafeClear (Histo-Clear)	Thermo Fisher Scientific	23-044-192
Epredia Shandon Bluing Reagent	Thermo Fisher Scientific	6769002
Permount	Thermo Fisher Scientific	SP15-100
Bouin's solution	Sigma-Aldrich	HT10132-1L
Douill's Solution	TI 5:1 6: .:0	NC9150318
HistoGel	Thermo Fisher Scientific	1403130310
	Promega	G3250



Table 1. Key Resources Table (Continued)

Reagent or resource	Source	Identifier
Paraformaldehyde	Electron Microscopy Sciences	19200
Kodak Professional Photo- Flo 200	Kodak	1464510
Goat serum, New Zealand origin	Thermo Fisher Scientific	16210072
Microscope slides, 6 well, 8 mm	Laborimpex (VWR)	63423-08 (100490-336)
Standard coverslips #1.5	VWR	152460 (16002- 268)
Bovine serum albumin	Sigma-Aldrich	A7906-500g
Triton X-100	Thermo Fisher Scientific	BP151-500
In vitro CHK1 inhibition		
Rabusertib (LY2603618)	Selleckchem	S2626
Leibovitz's L-15 Medium	Thermo Fisher Scientific	11415064
MEM α, nucleosides	Thermo Fisher Scientific	12571063
DMSO		
24-well plate		
Falcon Permeable Support for 24-well Plate with 3.0 µm Transparent PET Membrane, Sterile	Corning	353096
Experimental models: organis	ms and strains	
C57BL/6J	The Jackson Laboratory	#000664
Cntd1 ^{HA}	Gray et al. (2020), https://doi.org/10.1016/j.celrep. 2020.107858	Lead contact
Oligonucleotides (genotyping))	
Cntd1_HA_Fwd	5'-GCGCACGAGTGTTTG TGCACT-3'	IDT
Cntd1_HA_Rev	5'-CCAGTGACAAGGCAG TGCGGGTCAGCC-3'	IDT
Cntd1_mutant_Fwd	5'-CCAAGGTGTGGCAGA AGATTC-3'	IDT
Cntd1_mutant_Rev	5'-CGATAGTCTCTGTGG TAACCA-3'	IDT
Chk2_mutant_Fwd	5'-CCAAAGAAGTCTCCG TTGCT-3'	IDT
Chk2_mutant_Rev	5'-CAAATTAAGGGCCAG CTCATTC-3'	IDT
Chk2_wildtype_Fwd	5'-CCTTATGTGGTACGC CCACT-3'	IDT
		IDT

Table 1. Key Resources Table (Continued)

Reagent or resource	Source	Identifier
CNTD1-Flag-HA HDR Donor	5'-CCTGGGCCACAGCAG CCTGTTCCCCACAAGGCA GCCAGAGCTCTGAGGACT GCTGCCGCTGCCGCTTCC TCTAACACG-3', 5'-GAC TACAAAGACGATGACGAC AAGCTTT-3', 5'-ACCCAT ACGATGTTCCAGATTACG CTTGAGGGTGGCTGACCC GCACTGCCTTGTCACTGG-3', 5'-ACCTCTTTCCTTGTT TACTTTTATACTCAGGG-3'	IDT; Gray et al. (2020)
Cntd1-Flag-HA crRNA	5'-CGCUUCCUCUAACAC GUGA-3'	IDT; Gray et al. (2020)
Cntd1 mutant crRNA	5'-UAGUGACUUUCAGUU CGGAG-3'	IDT; Gray et al. (2020)
Cntd1-Flag-HA sequencing primer_Fwd	5'- GCGCACGAGTGTTTG TGCACT-3'	IDT; Gray et al. (2020)
Cntd1-Flag-HA sequencing primer_Rev	5'- CCAGTGACAAGGCAG TGCGGGTCAGCC-3'	IDT; Gray et al. (2020)
pX330	Addgene	42330
Oligonucleotides (Cloning)		
CNTD1_F	5'-TTTTGGATCCATGCT GAAGCAGGCAGAGGAC-3'	
CNTD1_R	5'-TTTTCTCGAGTCACG TGTTAGAGGAAGCGGC-3'	

CNTD1_R (see Key Resources Table [Table 1]) and cloned into pGEX-4T and pET-28a bacterial expression vectors using restriction digest (BamHI for forward primer, XhoI for reverse primer) to create a CNTD1-GST and CNTD1-6XHis recombinant protein, respectively. For expression of both CNTD1-GST and CNTD1-6XHis, constructs were transformed into BL21 E. coli, grown at 37°C until inducing with 0.5 mM IPTG, then grown for 3.5 h. The CNTD1-GST protein was purified into 100 mM GSH, 58 mM Na₂HPO₄, 17 mM NaH₂PO₄, 68 mM NaCl, pH 8.0, lyophilized, then reconstituted in sterile water before immunization of a rabbit. Production bleeds from the animals were obtained over ~3 mo and were tested by ELISA. Positive bleeds were purified using the recombinant purified CNTD1-6XHis protein. CNTD1-6XHis was purified into 300 mM imidazole, 58 mM Na₂HPO₄, 17 mM NaH₂PO₄, 68 mM NaCl, pH 7.4. The specificity of this antibody was tested in this study (Fig. S4).

Neonatal ovarian organ cultures in the presence of the CHK1 inhibitor

PND5 ovaries were dissected and cultured as published previously (Martínez-Marchal et al., 2020; Morgan et al., 2015). Briefly, tail snips were collected at the time of dissection for genotyping with Cntdl_HA primers. Ovaries were collected from PND5 females in dissection media (L15 media with 3 mg/ml of BSA). Ovaries were cultured with either 5 μ M of DMSO or CHK1i in α -MEM with 3 mg/ml BSA in a 24-well plate with a well



insert. Ovaries were cultured in an incubator at 37°C, supplied with 5% CO₂ for 5 days, with medium changes every 48 h. Ovaries were then fixed in formalin for 1 h at room temperature and outsourced to the Cornell Histology Core for subsequent sectioning at 5 µm per section. Sections were then deparaffinized with Histo-Clear and dehydrated through ethanol dilutions. Sections were processed for immunostaining with antigen retrieval in boiling sodium citrate buffer (trisodium citrate 10 mM, pH 6.0) for 30 min. Immunofluorescence was performed using rabbit anti-DDX4 (Cell Signaling) at 1:1,000 in 1X ADB at 37°C for 1 h and anti-rabbit Alexa Fluor 488 at 1:500 in 1X ADB for 1 h at 37°C. Slides were mounted with DAPI plus antifade and imaged utilizing a Zeiss Axiophot Z1 microscope at 10× magnification. Every fifth section was analyzed, and only DDX4positive oocytes with a visible nucleus were quantified. The total number of oocytes was multiplied by 5. $n \ge 3$ pairs of ovaries were used per genotype per condition group.

Ovarian immunofluorescence staining with tandem TUNEL staining

PND1 ovaries obtained from Cntd1HA/HA, Cntd1HA/-, and Cntd1-/animals were dissected and fixed in formalin for ${\sim}30$ min at room temperature with gentle rocking. The ovaries were then washed with 70% ethanol and embedded in HistoGel for processing by the Cornell Histology Core. Ovaries were paraffinembedded and subsequently sectioned at 5-µm intervals. For immunofluorescence staining, the ovaries were deparaffinized and processed through antigen retrieval with primary (antimouse MSY2 at 1:50) and secondary (anti-mouse Alexa Fluor 594 at 1:500) antibody staining as described above. All subsequent TUNEL staining was performed in the dark and according to the manufacturer's recommendation. Briefly, ovaries were fixed in 4% paraformaldehyde (pH 7.4) for 15 min at room temperature. The ovaries were then washed with 2 × 5-min washes in 1X PBS. 20 µg/ml of Proteinase K was added to each section followed by 1 × 5-min wash in 1X PBS. Ovaries were then fixed again in 4% PFA for 15 min followed by a 1 × 5-min wash in 1X PBS. An equilibration buffer was added to each section for 10 min. The slides were then labeled with TdT for 1 h. After, the slides were immersed in 2X SSC buffer for 15 min and washed three times for 5 min with 1X PBS. The slides were then immersed in 10 mM CuSO₄ and 50 mM NH₄Cl to prevent autofluorescence. The secondary antibody was added again, and the slides were left to incubate at 37°C for 30 min. The slides were then washed three times for 5 min and mounted with DAPI plus antifade and imaged at 63× magnification on a Zeiss Axiophot Z1 microscope.

Image acquisition and microscopy

Imaging was performed using a Zeiss Axiophot Z1 microscope (Zeiss Axio Imager 7.2) attached to a cooled charge-coupled device black and white camera (Zeiss McM) and AxioCam 503 Mono. All immunofluorescence images are from cells fixed on glass slides, mounted with DAPI with antifade (Materials), and sealed with a glass coverslip. Immunofluorescence images were captured at either 10× or 63× magnification (Plan-APOCHROMAT) at room temperature utilizing the following fluorochromes: DAPI,

secondary antibody-conjugated Alexa Fluor 488, secondary antibody-conjugated Alexa Fluor 594 or rhodamine, and secondary antibody-conjugated Alexa Fluor 647, and pseudocolored using ZEN 3.0 software (Carl Zeiss AG) The brightness and contrast of images were adjusted using ImageJ (Schindelin et al., 2012) (National Institutes of Health, Bethesda, MD, USA). Histology images were acquired using Aperio software using an Aperio CS2 Digital Pathology Slide Scanner microscope at 40× magnification.

Quantification and statistical analysis

Statistical analyses were performed using GraphPad Prism version 9.00 for Macintosh and Microsoft Excel. Specific analyses are described within the text and the corresponding figures. All datasets were analyzed for normality using a Shapiro–Wilk test. Alpha value was established at 0.05 for all statistical tests. The statistical tests utilized are included in the figure legends. All statistical analysis was monitored by the Cornell Statistical Consulting Unit.

Online supplemental material

Fig. S1 shows colocalization analysis of CNTD1 and MLH3 and a 3-mo breeding assay. Fig. S2 shows western blot and immunoprecipitation-western blot analyses of whole testis lysates for CNTD1 using custom and commercial CNTD1 antibodies. Fig. S3 shows progression through prophase I in Cntd1^{-/-} oocytes is altered at 17.5 dpc. Fig S4 shows early DSB repair in Cntd1^{-/-} oocytes is normal. Fig. S5 shows Cntd1^{-/-} ovaries have an increase in TUNEL-positive cells. Table S1 shows raw values, mean, and statistical results for Figs. 1, 4, 5, 6, and 7 in individual tabs. Table S2 shows raw oocyte and/or follicle counts and statistical results for Figs. 3, 8, and 9. Table S3 shows raw values, mean, and statistical results for Fig. S4.

Data availability

Lead contact

Further information and requests for resources and reagents should be directed to and will be fulfilled by the Lead Contact, Paula Cohen (paula.cohen@cornell.edu).

Materials availability

Mouse lines generated within this study are available upon request from the Lead Contact, Paula Cohen (paula.cohen@cornell.edu).

Acknowledgments

We thank the Cohen laboratory for support during these studies. We also thank Dr. Carolline Ascenção and Dr. Ewelina Bolcun-Filas for experimental help, Dr. Attila Tóth (Technische Universitat Dresden, Dresden, Germany) for CNTD1 antibodies, the Cornell Stem Cell and Transgenic Core for creating mouse lines, CARE staff for mouse care and husbandry, and Dr. Matthew Thomas (Cornell Statistical Consulting Unit) for data analysis.

Funding for this research was provided by grants from the National Institutes of Health to P.E. Cohen (R01HD041012,

https://doi.org/10.1083/jcb.202401021



R01HD097987), I.D. Wolff (F32HD106630), and S. Gray. (K99HD092618), and the Natural Sciences and Engineering Research Council of Canada to R.A. Bradley (PGSD-577969).

Author contributions: A.J. Wood: conceptualization, data curation, formal analysis, investigation, methodology, validation, visualization, and writing—original draft, review, and editing. R.M. Ahmed: data curation, formal analysis, investigation, and writing—review and editing. L.E. Simon: investigation and methodology. R.A. Bradley: formal analysis. S. Gray: investigation and resources. I.D. Wolff: conceptualization, funding acquisition, investigation, methodology, project administration, resources, supervision, validation, visualization, and writing—original draft, review, and editing. P.E. Cohen: conceptualization, methodology, project administration, resources, supervision, and writing—original draft, review, and editing.

Disclosures: The authors declare no competing interests exist.

Submitted: 4 January 2024 Revised: 4 March 2025 Accepted: 19 May 2025

References

- Alexander, A.K., E.J. Rice, J. Lujic, L.E. Simon, S. Tanis, G. Barshad, L. Zhu, J. Lama, P.E. Cohen, and C.G. Danko. 2023. A-MYB and BRDT-dependent RNA Polymerase II pause release orchestrates transcriptional regulation in mammalian meiosis. *Nat. Commun.* 14:1753. https://doi.org/10.1038/s41467-023-37408-w
- Baker, T.G. 1963. A quantitative and cytological study of germ cells in human ovaries. Proc. R. Soc. Lond. B. 158:417–433. https://doi.org/10.1098/rspb .1963.0055
- Bishop, D.K., D. Park, L. Xu, and N. Kleckner. 1992. DMC1: A meiosis-specific yeast homolog of *E. coli* recA required for recombination, synaptonemal complex formation, and cell cycle progression. *Cell*. 69:439–456. https://doi.org/10.1016/0092-8674(92)90446-j
- Blundon, J.M., B.I. Cesar, J.W. Bae, I. Čavka, J. Haversat, J. Ries, S. Köhler, and Y. Kim. 2024. Skp1 proteins are structural components of the synaptonemal complex in C. elegans. Sci. Adv. 10:eadl4876. https://doi.org/10 .1126/sciady.adl4876
- Bolcun-Filas, E., V.D. Rinaldi, M.E. White, and J.C. Schimenti. 2014. Reversal of female infertility by Chk2 ablation reveals the oocyte DNA damage checkpoint pathway. *Science*. 343:533–536. https://doi.org/10.1126/science.1247671
- Bondarieva, A., K. Raveendran, V. Telychko, H.B.D.P. Rao, R. Ravindranathan, C. Zorzompokou, F. Finsterbusch, I. Dereli, F. Papanikos, D. Tränkner, et al. 2020. Proline-rich protein PRR19 functions with cyclin-like CNTD1 to promote meiotic crossing over in mouse. *Nat. Commun.* 11: 3101. https://doi.org/10.1038/s41467-020-16885-3
- Borum, K. 1961. Oogenesis in the mouse. A study of the meiotic prophase. *Exp. Cell Res.* 24:495–507. https://doi.org/10.1016/0014-4827(61)90449-9
- Cao, L., E. Alani, and N. Kleckner. 1990. A pathway for generation and processing of double-strand breaks during meiotic recombination in S. cerevisiae. Cell. 61:1089–1101. https://doi.org/10.1016/0092-8674(90) 90072-m
- Chen, L., S.-B. Chao, Z.-B. Wang, S.-T. Qi, X.-L. Zhu, S.-W. Yang, C.-R. Yang, Q.-H. Zhang, Y.-C. Ouyang, Y. Hou, et al. 2012. Checkpoint kinase 1 is essential for meiotic cell cycle regulation in mouse oocytes. *Cell Cycle*. 11: 1948–1955. https://doi.org/10.4161/cc.20279
- Chotiner J.Y., Leu N.A., Yang F., Cossu I.G., Guan Y., Lin H., Wang P.J.. 2023. TRIP13 localizes to synapsed chromosomes and functions as a dosage-sensitive regulator of meiosis. *Elife*. 12:RP92195. https://doi.org/10.7554/eLife.92195.1
- Cloud, V., Y.-L. Chan, J. Grubb, B. Budke, and D.K. Bishop. 2012. Rad51 is an accessory factor for Dmc1-mediated joint molecule formation during meiosis. Science. 337:1222–1225. https://doi.org/10.1126/science.1219379

- Collins, P.L., C. Purman, S.I. Porter, V. Nganga, A. Saini, K.E. Hayer, G.L. Gurewitz, B.P. Sleckman, J.J. Bednarski, C.H. Bassing, and E.M. Oltz. 2020. DNA double-strand breaks induce H2Ax phosphorylation domains in a contact-dependent manner. *Nat. Commun.* 11:3158. https://doi.org/10.1038/s41467-020-16926-x
- Condezo, Y.A., R. Sainz-Urruela, L. Gomez-H, D. Salas-Lloret, N. Felipe-Medina, R. Bradley, I.D. Wolff, S. Tanis, J.L. Barbero, M. Sánchez-Martín, et al. 2024. RNF212B E3 ligase is essential for crossover designation and maturation during male and female meiosis in the mouse. *Proc. Natl. Acad. Sci. USA*. 121:e2320995121. https://doi.org/10.1073/pnas.2320995121
- de Vries, S.S., E.B. Baart, M. Dekker, A. Siezen, D.G. de Rooij, P. de Boer, and H. te Riele. 1999. Mouse MutS-like protein Msh5 is required for proper chromosome synapsis in male and female meiosis. *Genes Dev.* 13: 523-531. https://doi.org/10.1101/gad.13.5.523
- Di Giacomo, M., M. Barchi, F. Baudat, W. Edelmann, S. Keeney, and M. Jasin. 2005. Distinct DNA-damage-dependent and -independent responses drive the loss of oocytes in recombination-defective mouse mutants. *Proc. Natl. Acad. Sci. USA*. 102:737–742. https://doi.org/10.1073/pnas.0406212102
- Edelmann, W., P.E. Cohen, M. Kane, K. Lau, B. Morrow, S. Bennett, A. Umar, T. Kunkel, G. Cattoretti, R. Chaganti, et al. 1996. Meiotic pachytene arrest in MLH1-deficient mice. *Cell*. 85:1125–1134. https://doi.org/10.1016/s0092-8674(00)81312-4
- Edelmann, W., P.E. Cohen, B. Kneitz, N. Winand, M. Lia, J. Heyer, R. Kolodner, J.W. Pollard, and R. Kucherlapati. 1999. Mammalian MutS homologue 5 is required for chromosome pairing in meiosis. *Nat. Genet.* 21: 123–127. https://doi.org/10.1038/5075
- Epifano, O., and J. Dean. 2002. Genetic control of early folliculogenesis in mice. Trends Endocrinol. Metab. 13:169–173. https://doi.org/10.1016/s1043-2760(02)00576-3
- Goetz, P., A.C. Chandley, and R.M. Speed. 1984. Morphological and temporal sequence of meiotic prophase development at puberty in the male mouse. J. Cell Sci. 65:249–263. https://doi.org/10.1242/jcs.65.1.249
- Gray, S., and P.E. Cohen. 2016. Control of meiotic crossovers: From double-strand break formation to designation. Annu. Rev. Genet. 50:175–210. https://doi.org/10.1146/annurev-genet-120215-035111
- Gray, S., E.R. Santiago, J.S. Chappie, and P.E. Cohen. 2020. Cyclin N-terminal domain-containing-1 coordinates meiotic crossover formation with cell-cycle progression in a cyclin-independent manner. *Cell Rep.* 32: 107858. https://doi.org/10.1016/j.celrep.2020.107858
- Gruhn, J.R., and E.R. Hoffmann. 2022. Errors of the egg: The establishment and progression of human aneuploidy research in the maternal germline. *Annu. Rev. Genet.* 56:369–390. https://doi.org/10.1146/annurev-genet-072820-033609
- Gruhn, J.R., C. Rubio, K.W. Broman, P.A. Hunt, and T. Hassold. 2013. Cytological studies of human meiosis: Sex-specific differences in recombination originate at, or prior to, establishment of double-strand breaks. PLoS One. 8:e85075. https://doi.org/10.1371/journal.pone.0085075
- Guan, Y., N.A. Leu, J. Ma, L. Chmátal, G. Ruthel, J.C. Bloom, M.A. Lampson, J.C. Schimenti, M. Luo, and P.J. Wang. 2020. SKP1 drives the prophase I to metaphase I transition during male meiosis. Sci. Adv. 6:eaaz2129. https://doi.org/10.1126/sciadv.aaz2129
- Guan, Y., H. Lin, N.A. Leu, G. Ruthel, S.Y. Fuchs, L. Busino, M. Luo, and P.J. Wang. 2022. SCF ubiquitin E3 ligase regulates DNA doublestrand breaks in early meiotic recombination. *Nucleic Acids Res*. 50:5129-5144. https://doi.org/10.1093/nar/gkac304
- Guo, T., S. Zhao, S. Zhao, M. Chen, G. Li, X. Jiao, Z. Wang, Y. Zhao, Y. Qin, F. Gao, and Z.-J. Chen. 2017. Mutations in MSH5 in primary ovarian insufficiency. Hum. Mol. Genet. 26:1452–1457. https://doi.org/10.1093/hmg/ddx044
- Hamer, G., H. Wang, E. Bolcun-Filas, H.J. Cooke, R. Benavente, and C. Höög. 2008. Progression of meiotic recombination requires structural maturation of the central element of the synaptonemal complex. J. Cell Sci. 121:2445–2451. https://doi.org/10.1242/jcs.033233
- Hassold, T., and P. Hunt. 2001. To err (meiotically) is human: The genesis of human aneuploidy. Nat. Rev. Genet. 2:280-291. https://doi.org/10.1038/ 35066065
- Hassold, T., H. Maylor-Hagen, A. Wood, J. Gruhn, E. Hoffmann, K.W. Broman, and P. Hunt. 2021. Failure to recombine is a common feature of human oogenesis. Am. J. Hum. Genet. 108:16-24. https://doi.org/10.1016/j.ajhg.2020.11.010
- Haversat, J., A. Woglar, K. Klatt, C.C. Akerib, V. Roberts, S.-Y. Chen, S. Arur, A.M. Villeneuve, and Y. Kim. 2022. Robust designation of meiotic crossover sites by CDK-2 through phosphorylation of the MutSγ complex. Proc. Natl. Acad. Sci. USA. 119:e2117865119. https://doi.org/10.1073/ pnas.2117865119



- Hinch, A.G., P.W. Becker, T. Li, D. Moralli, G. Zhang, C. Bycroft, C. Green, S. Keeney, Q. Shi, B. Davies, and P. Donnelly. 2020. The configuration of RPA, RAD51, and DMC1 binding in meiosis reveals the nature of critical recombination intermediates. *Mol. Cell*. 79:689–701.e10. https://doi.org/10.1016/j.molcel.2020.06.015
- Holloway, J.K., J. Booth, W. Edelmann, C.H. McGowan, and P.E. Cohen. 2008. MUS81 generates a subset of MLH1-MLH3-independent crossovers in mammalian meiosis. PLoS Genet. 4:e1000186. https://doi.org/10.1371/journal.pgen.1000186
- Holloway, J.K., X. Sun, R. Yokoo, A.M. Villeneuve, and P.E. Cohen. 2014. Mammalian CNTD1 is critical for meiotic crossover maturation and deselection of excess precrossover sites. J. Cell Biol. 205:633-641. https://doi.org/10.1083/jcb.201401122
- Huang, C., T. Guo, and Y. Qin. 2021. Meiotic recombination defects and premature ovarian insufficiency. Front. Cell Dev. Biol. 9:652407. https:// doi.org/10.3389/fcell.2021.652407
- Huang, Y., and I. Roig. 2023. Genetic control of meiosis surveillance mechanisms in mammals. Front. Cell Dev. Biol. 11:1127440. https://doi.org/10.3389/fcell.2023.1127440
- Hunter, N. 2015. Meiotic recombination: The essence of heredity. Cold Spring Harb. Perspect. Biol. 7:a016618. https://doi.org/10.1101/ cshperspect.a016618
- Hunt, P.A., and T.J. Hassold. 2008. Human female meiosis: What makes a good egg go bad? Trends Genet. 24:86-93. https://doi.org/10.1016/j.tig .2007.11.010
- Hwang, G.H., J.L. Hopkins, and P.W. Jordan. 2018. Chromatin spread preparations for the analysis of mouse oocyte progression from prophase to metaphase II. J. Vis. Exp. 132:e56736. https://doi.org/10.3791/56736
- Ito, M., Y. Yun, D.S. Kulkarni, S. Sandhu, B. Nuñez, L. Hu, K. Lee, N. Lim, R. Hirota, R. Prendergast, et al. 2023. Distinct and interdependent functions of three RING proteins regulate recombination during mammalian meiosis. bioRxiv. https://doi.org/10.1101/2023.11.07.566091 (Preprint posted November 10, 2023).
- Kan, R., X. Sun, N.K. Kolas, E. Avdievich, B. Kneitz, W. Edelmann, and P.E. Cohen. 2008. Comparative analysis of meiotic progression in female mice bearing mutations in genes of the DNA mismatch repair pathway. Biol. Reprod. 78:462-471. https://doi.org/10.1095/biolreprod.107.065771
- Ke, H., S. Tang, T. Guo, D. Hou, X. Jiao, S. Li, W. Luo, B. Xu, S. Zhao, G. Li, et al. 2023. Landscape of pathogenic mutations in premature ovarian insufficiency. *Nat. Med.* 29:483–492. https://doi.org/10.1038/s41591-022-02194-3
- Keeney, S., C.N. Giroux, and N. Kleckner. 1997. Meiosis-specific DNA double-strand breaks are catalyzed by Spo11, a member of a widely conserved protein family. Cell. 88:375–384. https://doi.org/10.1016/s0092-8674(00)81876-0
- King, C., H. Diaz, D. Barnard, D. Barda, D. Clawson, W. Blosser, K. Cox, S. Guo, and M. Marshall. 2014. Characterization and preclinical development of LY2603618: A selective and potent Chkl inhibitor. *Invest. New Drugs*. 32: 213–226. https://doi.org/10.1007/s10637-013-0036-7
- Kneitz, B., P.E. Cohen, E. Avdievich, L. Zhu, M.F. Kane, H. Hou Jr., R.D. Kolodner, R. Kucherlapati, J.W. Pollard, and W. Edelmann. 2000. MutS homolog 4 localization to meiotic chromosomes is required for chromosome pairing during meiosis in male and female mice. *Genes Dev.* 14: 1085–1097. https://doi.org/10.1101/gad.14.9.1085
- Kogo, H., M. Tsutsumi, T. Ohye, H. Inagaki, T. Abe, and H. Kurahashi. 2012. HORMAD1-dependent checkpoint/surveillance mechanism eliminates asynaptic oocytes. *Genes Cells*. 17:439–454. https://doi.org/10.1111/j.1365 -2443.2012.01600.x
- Lenzi, M.L., J. Smith, T. Snowden, M. Kim, R. Fishel, B.K. Poulos, and P.E. Cohen. 2005. Extreme heterogeneity in the molecular events leading to the establishment of chiasmata during meiosis i in human oocytes. Am. J. Hum. Genet. 76:112–127. https://doi.org/10.1086/427268
- Lipkin, S.M., P.B. Moens, V. Wang, M. Lenzi, D. Shanmugarajah, A. Gilgeous, J. Thomas, J. Cheng, J.W. Touchman, E.D. Green, et al. 2002. Meiotic arrest and aneuploidy in MLH3-deficient mice. *Nat. Genet.* 31:385–390. https://doi.org/10.1038/ng931
- Liu, Q., S. Guntuku, X.S. Cui, S. Matsuoka, D. Cortez, K. Tamai, G. Luo, S. Carattini-Rivera, F. DeMayo, A. Bradley, et al. 2000. Chk1 is an essential kinase that is regulated by Atr and required for the G(2)/M DNA damage checkpoint. Genes Dev. 14:1448-1459. https://doi.org/10.1101/gad.14.12.1448
- MacQueen, A.J. 2015. Catching a (Double-Strand) break: The Rad51 and Dmc1 strand exchange proteins can co-occupy both ends of a meiotic DNA double-strand break. PLoS Genet. 11:e1005741. https://doi.org/10.1371/ journal.pgen.1005741

CNTD1 is critical for meiosis in female mice

- Martínez-Marchal, A., Y. Huang, M.T. Guillot-Ferriols, M. Ferrer-Roda, A. Guixé, M. Garcia-Caldés, and I. Roig. 2020. The DNA damage response is required for oocyte cyst breakdown and follicle formation in mice. *PLoS Genet.* 16:e1009067. https://doi.org/10.1371/journal.pgen.1009067
- Menke, D.B., J. Koubova, and D.C. Page. 2003. Sexual differentiation of germ cells in XX mouse gonads occurs in an anterior-to-posterior wave. *Dev. Biol.* 262:303–312. https://doi.org/10.1016/S0012-1606(03)00391-9
- Mihalas, B.P., G.H. Pieper, M. Aboelenain, L. Munro, V. Srsen, C.E. Currie, D.A. Kelly, G.M. Hartshorne, E.E. Telfer, A.D. McAinsh, et al. 2024. Agedependent loss of cohesion protection in human oocytes. *Curr. Biol.* 34: 117–131.e5. https://doi.org/10.1016/j.cub.2023.11.061
- Milano, C.R., J.K. Holloway, Y. Zhang, B. Jin, C. Smith, A. Bergman, W. Edelmann, and P.E. Cohen. 2019. Mutation of the ATPase domain of MutS Homolog-5 (MSH5) reveals a requirement for a functional MutSγ complex for all crossovers in mammalian meiosis. G3 (Bethesda). 9: 1839–1850. https://doi.org/10.1534/g3.119.400074
- Morelli, M.A., and P.E. Cohen. 2005. Not all germ cells are created equal: Aspects of sexual dimorphism in mammalian meiosis. Reproduction. 130: 761–781. https://doi.org/10.1530/rep.1.00865
- Morelli, M.A., U. Werling, W. Edelmann, M.S. Roberson, and P.E. Cohen. 2008. Analysis of meiotic prophase I in live mouse spermatocytes. *Chromosome Res.* 16:743–760. https://doi.org/10.1007/s10577-008-1224-8
- Morgan, S., L. Campbell, V. Allison, A. Murray, and N. Spears. 2015. Culture and co-culture of mouse ovaries and ovarian follicles. *J. Vis. Exp.* 52458. https://doi.org/10.3791/52458
- Nagaoka, S.I., T.J. Hassold, and P.A. Hunt. 2012. Human aneuploidy: Mechanisms and new insights into an age-old problem. Nat. Rev. Genet. 13: 493-504. https://doi.org/10.1038/nrg3245
- Palmer, N., S.Z.A. Talib, P. Singh, C.M.F. Goh, K. Liu, J.C. Schimenti, and P. Kaldis. 2020. A novel function for CDK2 activity at meiotic crossover sites. PLoS Biol. 18:e3000903. https://doi.org/10.1371/ journal.pbio.3000903
- Pittman, D.L., J. Cobb, K.J. Schimenti, L.A. Wilson, D.M. Cooper, E. Brignull, M.A. Handel, and J.C. Schimenti. 1998. Meiotic prophase arrest with failure of chromosome synapsis in mice deficient for Dmc1, a germlinespecific RecA homolog. Mol. Cell. 1:697-705. https://doi.org/10.1016/ s1097-2765(00)80069-6
- Qiao, H., H.B.D. Prasada Rao, Y. Yang, J.H. Fong, J.M. Cloutier, D.C. Deacon, K.E. Nagel, R.K. Swartz, E. Strong, J.K. Holloway, et al. 2014. Antagonistic roles of ubiquitin ligase HEIIO and SUMO ligase RNF212 regulate meiotic recombination. Nat. Genet. 46:194–199. https://doi.org/10.1038/ng.2858
- Qiao, H., H.B.D.P. Rao, Y. Yun, S. Sandhu, J.H. Fong, M. Sapre, M. Nguyen, A. Tham, B.W. Van, T.Y.H. Chng, et al. 2018. Impeding DNA break repair enables oocyte quality control. *Mol. Cell.* 72:211–221.e3. https://doi.org/10.1016/j.molcel.2018.08.031
- Ravindranathan, R., K. Raveendran, F. Papanikos, P.A. San-Segundo, and A. Tóth. 2022. Chromosomal synapsis defects can trigger oocyte apoptosis without elevating numbers of persistent DNA breaks above wild-type levels. Nucleic Acids Res. 50:5617–5634. https://doi.org/10.1093/nar/gkac355
- Reynolds, A., H. Qiao, Y. Yang, J.K. Chen, N. Jackson, K. Biswas, J.K. Holloway, F. Baudat, B. de Massy, J. Wang, et al. 2013. RNF212 is a dosage-sensitive regulator of crossing-over during mammalian meiosis. *Nat. Genet.* 45: 269–278. https://doi.org/10.1038/ng.2541
- Rinaldi, V.D., J.C. Bloom, and J.C. Schimenti. 2020. Oocyte elimination through DNA damage signaling from CHK1/CHK2 to p53 and p63. Genetics. 215:373-378. https://doi.org/10.1534/genetics.120.303182
- Rinaldi, V.D., E. Bolcun-Filas, H. Kogo, H. Kurahashi, and J.C. Schimenti. 2017. The DNA damage checkpoint eliminates mouse oocytes with chromosome synapsis failure. Mol. Cell. 67:1026–1036.e2. https://doi.org/10.1016/j.molcel.2017.07.027
- Romanienko, P.J., and R.D. Camerini-Otero. 2000. The mouse Spo11 gene is required for meiotic chromosome synapsis. *Mol. Cell.* 6:975–987. https://doi.org/10.1016/s1097-2765(00)00097-6
- Sarma, U.C., A.L. Winship, and K.J. Hutt. 2020. Comparison of methods for quantifying primordial follicles in the mouse ovary. J. Ovarian Res. 13: 121. https://doi.org/10.1186/s13048-020-00724-6
- Schindelin, J., I. Arganda-Carreras, E. Frise, V. Kaynig, M. Longair, T. Pietzsch, S. Preibisch, C. Rueden, S. Saalfeld, B. Schmid, et al. 2012. Fiji: An open-source platform for biological-image analysis. *Nat. Methods.* 9: 676–682. https://doi.org/10.1038/nmeth.2019
- Shin, Y.-H., M.M. McGuire, and A. Rajkovic. 2013. Mouse HORMAD1 is a meiosis i checkpoint protein that modulates DNA double- strand break repair during female meiosis. Biol. Reprod. 89:29. https://doi.org/10 .1095/biolreprod.112.106773



- Speed, R.M. 1982. Meiosis in the foetal mouse ovary. I. An analysis at the light microscope level using surface-spreading. Chromosoma. 85:427-437. https://doi.org/10.1007/BF00330366
- Sun, X., and P.E. Cohen. 2013. Studying recombination in mouse oocytes. Methods Mol. Biol. 957:1-18. https://doi.org/10.1007/978-1-62703-191-2_1
- Tingen, C., A. Kim, and T.K. Woodruff. 2009a. The primordial pool of follicles and nest breakdown in mammalian ovaries. Mol. Hum. Reprod. 15: 795-803. https://doi.org/10.1093/molehr/gap073
- Tingen, C.M., S.K. Bristol-Gould, S.E. Kiesewetter, J.T. Wellington, L. Shea, and T.K. Woodruff. 2009b. Prepubertal primordial follicle loss in mice is not due to classical apoptotic pathways. Biol. Reprod. 81:16-25. https:// doi.org/10.1095/biolreprod.108.074898
- Tran, T.N., and J.C. Schimenti. 2019. A segregating human allele of SPO11 modeled in mice disrupts timing and amounts of meiotic recombination, causing oligospermia and a decreased ovarian reservet. Biol. Reprod. 101:347-359. https://doi.org/10.1093/biolre/ioz089
- Veitia, R.A. 2020. Primary ovarian insufficiency, meiosis and DNA repair. Biomed. J. 43:115-123. https://doi.org/10.1016/j.bj.2020.03.005
- Wang, S., T. Hassold, P. Hunt, M.A. White, D. Zickler, N. Kleckner, and L. Zhang. 2017. Inefficient crossover maturation underlies elevated aneuploidy in human female meiosis. Cell. 168:977-989.e17. https://doi .org/10.1016/j.cell.2017.02.002
- Wang, X., and M.E. Pepling. 2021. Regulation of meiotic prophase one in mammalian oocytes. Front. Cell Dev. Biol. 9:667306. https://doi.org/10 .3389/fcell.2021.667306

- Ward, J.O., L.G. Reinholdt, W.W. Motley, L.M. Niswander, D.C. Deacon, L.B. Griffin, K.K. Langlais, V.L. Backus, K.J. Schimenti, M.J. O'Brien, et al. 2007. Mutation in mouse hei10, an e3 ubiquitin ligase, disrupts meiotic crossing over. PLoS Genet. 3:e139. https://doi.org/10.1371/journal.pgen .0030139
- Woods, L.M., C.A. Hodges, E. Baart, S.M. Baker, M. Liskay, and P.A. Hunt. 1999. Chromosomal influence on meiotic spindle assembly: abnormal meiosis I in female Mlh1 mutant mice. J. Cell Biol. 145:1395-1406. https:// doi.org/10.1083/jcb.145.7.1395
- Yokoo, R., K.A. Zawadzki, K. Nabeshima, M. Drake, S. Arur, and A.M. Villeneuve. 2012. COSA-1 reveals robust homeostasis and separable licensing and reinforcement steps governing meiotic crossovers. Cell. 149:75-87. https://doi.org/10.1016/j.cell.2012.01.052
- Yoshida, K., G. Kondoh, Y. Matsuda, T. Habu, Y. Nishimune, and T. Morita. 1998. The mouse RecA-like gene Dmc1 is required for homologous chromosome synapsis during meiosis. Mol. Cell. 1:707-718. https://doi .org/10.1016/s1097-2765(00)80070-2
- Yuan, L., J.G. Liu, J. Zhao, E. Brundell, B. Daneholt, and C. Höög. 2000. The murine SCP3 gene is required for synaptonemal complex assembly, chromosome synapsis, and male fertility. Mol. Cell. 5:73-83. https://doi .org/10.1016/S1097-2765(00)80404-9
- Zhang, L., W. Stauffer, D. Zwicker, and A.F. Dernburg. 2021. Crossover patterning through kinase-regulated condensation and coarsening of recombination nodules. bioRxiv. https://doi.org/10.1101/2021.08.26 .457865 (Preprint posted August 27, 2021).

Wood et al. Journal of Cell Biology CNTD1 is critical for meiosis in female mice



Supplemental material

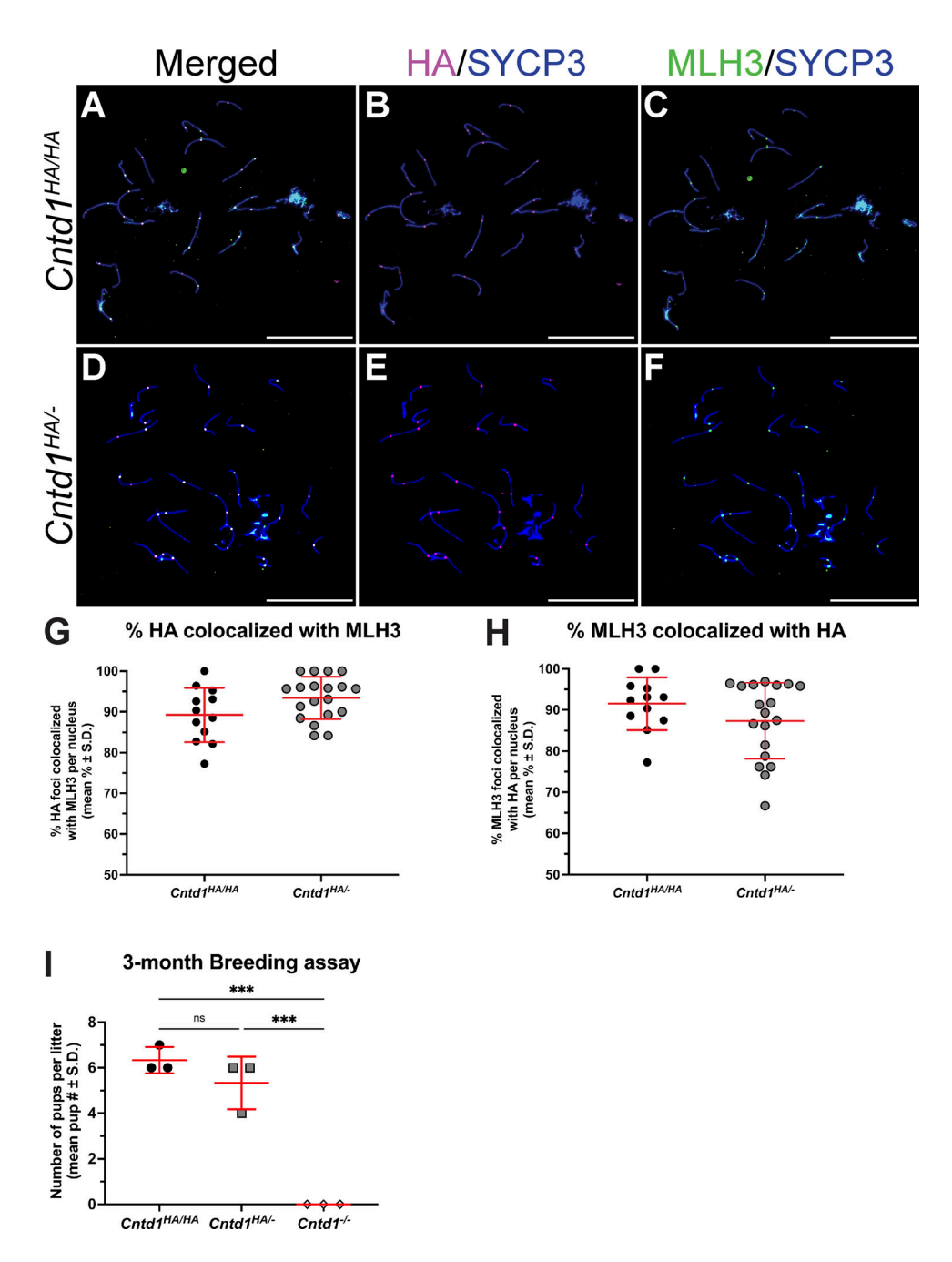


Figure S1. **Colocalization analysis of CNTD1 and MLH3 and a 3-mo breeding assay. (A-F)** Representative images of (A-C) $Cntd1^{HA/HA}$ (n = 12 nuclei) and (D-F) $Cntd1^{HA/-}$ (n = 19 nuclei) pachytene-staged oocytes ($n \ge 3$ fetal ovaries) stained for HA (magenta), MLH3 (green), and SYCP3 (blue). Images are representative of experiments from $n \ge 3$ fetuses. The average percentage of colocalization for $Cntd1^{HA/HA}$ and $Cntd1^{HA/-}$ of MLH3 with HA is 91.53% and 87.34%, respectively. **(G and H)** Quantification of colocalization. The average percentage of colocalization for $Cntd1^{HA/HA}$ and $Cntd1^{HA/-}$ of HA with MLH3 is 89.27% and 93.44%, respectively. The mean and standard deviation lines are in red. **(i)** 3-mo trio breeding assay of $Cntd1^{HA/HA}$ (black circles), $Cntd1^{HA/-}$ (gray squares), and $Cntd1^{-/-}$ (white diamonds) females housed with a $Cntd1^{HA/HA}$ male. Total pup numbers per litter are recorded for each dam genotype. $n \ge 3$ females were used per genotype. The mean and standard deviation lines are in red. Scale bars are equal to 20 μ m.

S2



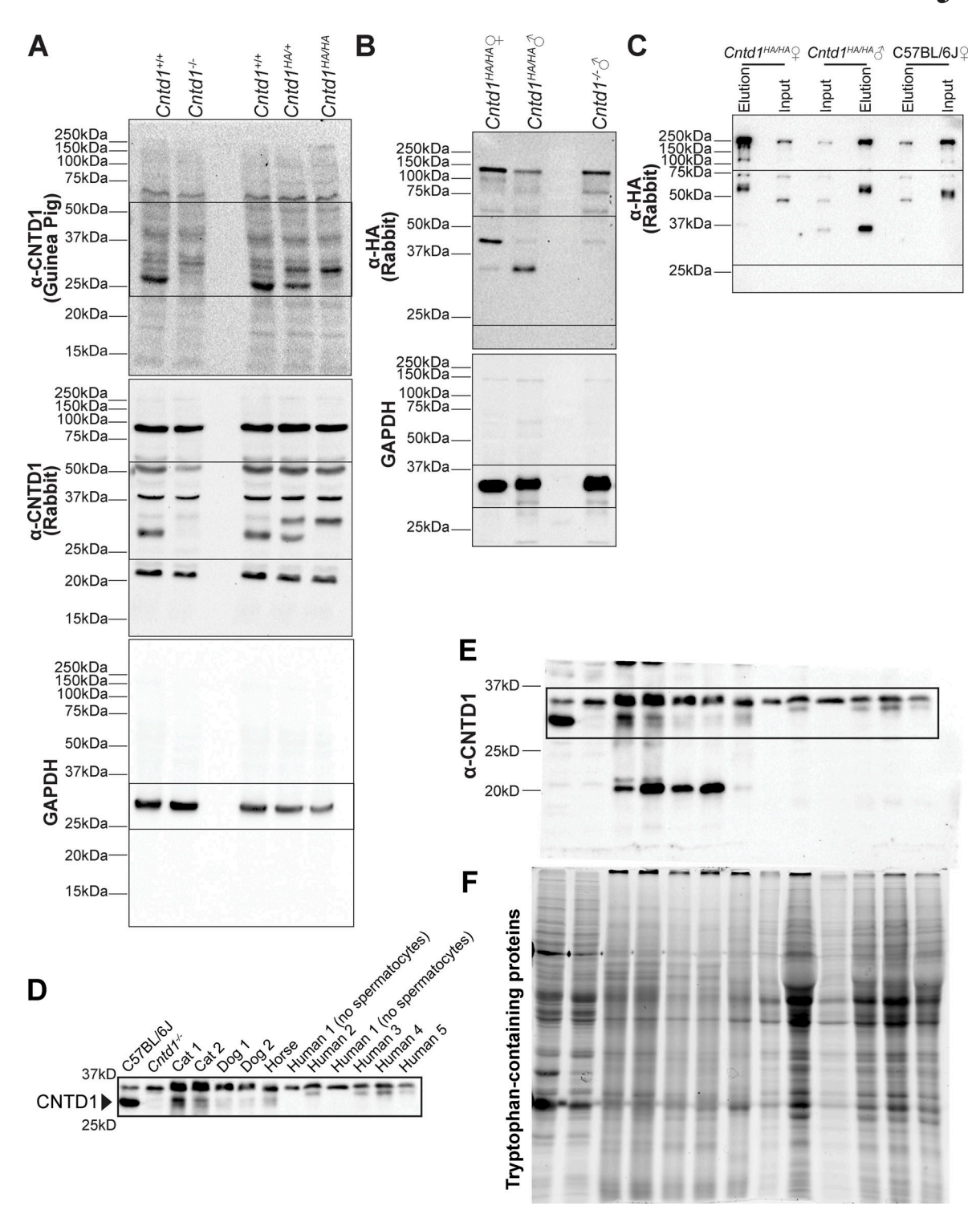


Figure S2. Western blot and immunoprecipitation-western blot analyses of whole testis lysates for CNTD1 using custom and commercial CNTD1 antibodies. Uncropped western blots used for Fig. 2. (A) Uncropped blot of Fig. 2 B. Anti-guinea pig CNTD1 (top) and anti-rabbit CNTD1 (middle) antibodies from Bondarieva et al. (2020) (https://doi.org/10.1038/s41467-020-16885-3) against whole testis lysates from Cntd1 mutant and Cntd1 FLAG-HA-tagged animals. GAPDH was used as a loading control (bottom). (B) Uncropped blot of Fig. 2 C. Western blot analysis of whole ovary lysates from 18.5 dpc Cntd1HA/HA and whole testis lysates from Cntd1^{HA/HA} and Cntd1^{-/-} animals probed with an anti-HA (rabbit) antibody with GAPDH loading control (bottom). (C) Uncropped blot of Fig. 2 D. Immunoprecipitation-western blot with whole ovary lysates from 18.5 dpc Cntd1HA/HA and C57BL/6J fetuses and whole testis lysate from Cntd1^{HA/HA}. CNTD1 was immunoprecipitated using anti-HA-conjugated magnetic beads, and western blotting was performed with an anti-HA (rabbit) antibody. (D) Cropped portion of E in the same figure. Western blot against whole testis lysates from C57BL/6, Cntd1-/-, cat, dog, horse, and human. Highlighted portion of western blot showing the presence of the CNTD1 band (black arrow) present in C57BL/6J, Cat 1, Cat 2, Dog 1, Dog 1, Horse, Human 2, Human 4, and Human 5 protein samples at or around the expected molecular weight, consistent with our previous report (Gray et al., 2020). (E) Whole image of western blot probed with the custom CNTD1 antibody seen in D. (F) TCE staining of SDS-PAGE gel for D and E. Black bounding boxes represent the portions highlighted in Fig. 2. TCE, trichloroethanol. Source data are available for this figure: SourceData FS2.

Wood et al. Journal of Cell Biology https://doi.org/10.1083/jcb.202401021



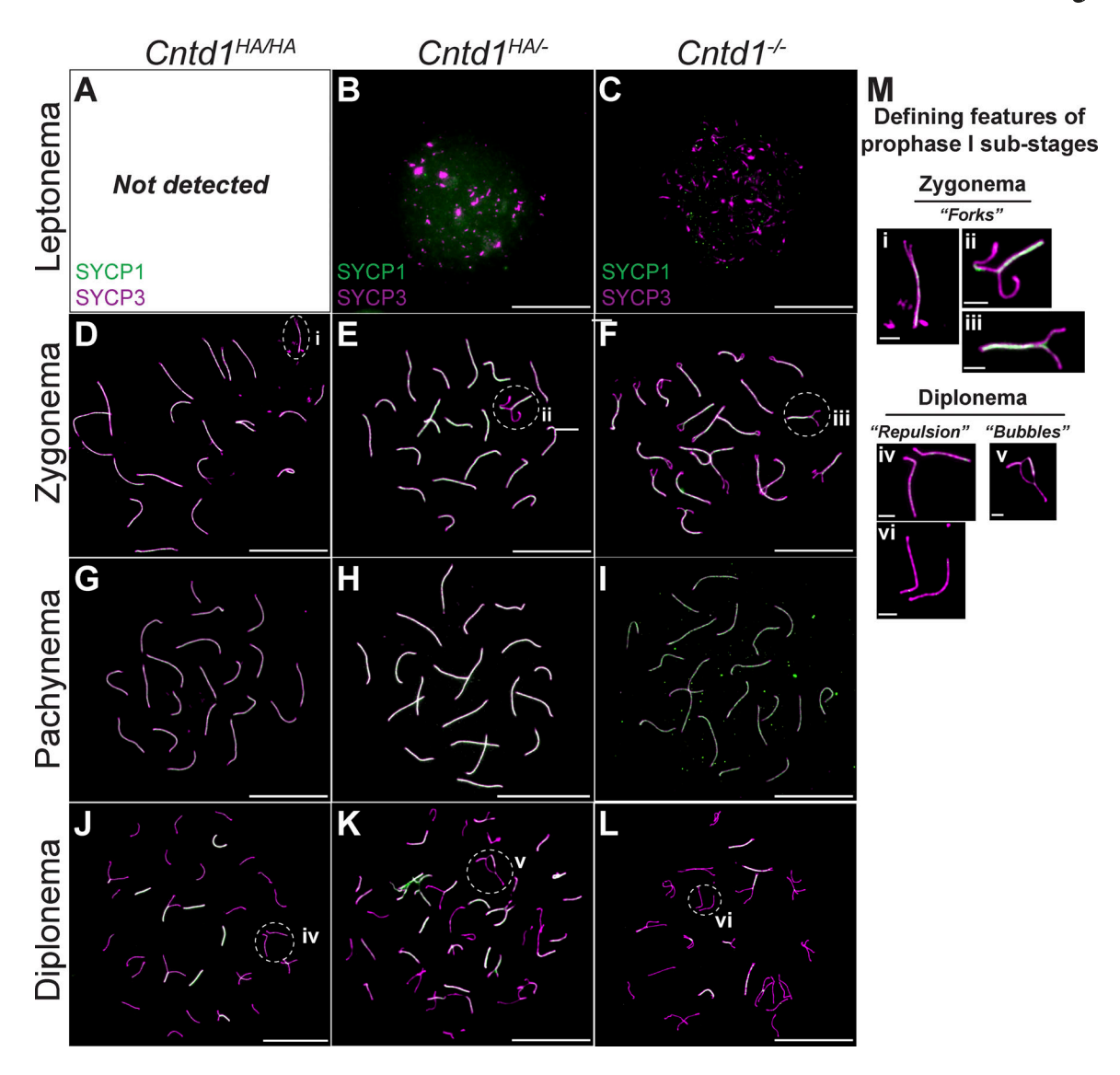


Figure S3. **Progression through prophase I in** *Cntd1*^{-/-} **oocytes is altered at 17.5 dpc. (A–L)** Localization of SYCP1 (green) and SYCP3 (magenta) on chromosome spreads from *Cntd1*^{HA/HA}, *Cntd1*^{HA/-}, and *Cntd1*^{-/-} oocytes at leptonema (A–C), zygonema (D–F), pachynema (G–I), and diplonema (J–L), using antibodies against each protein raised in rabbit (SYCP1) and mouse (SYCP3), respectively. **(M)** Examples of defining features of prophase I substages for zygonema and diplonema. (i–iii) Forks characteristic of zygonema-staged oocytes with colocalization of SYCP1 and SYCP3. (iv and vi) "Repulsion" and (v) bubbles, which are hallmark characteristics of diplonema-staged oocytes. Quantification of progression analysis shown in Fig. 6 M. White scale bars are equal to 20 μm, and inset scale bars (i–vi) are equal to 2 μm. A chi-square test was used to assess significance (****P < 0.0001). Statistics can be found in Table S1.

S3



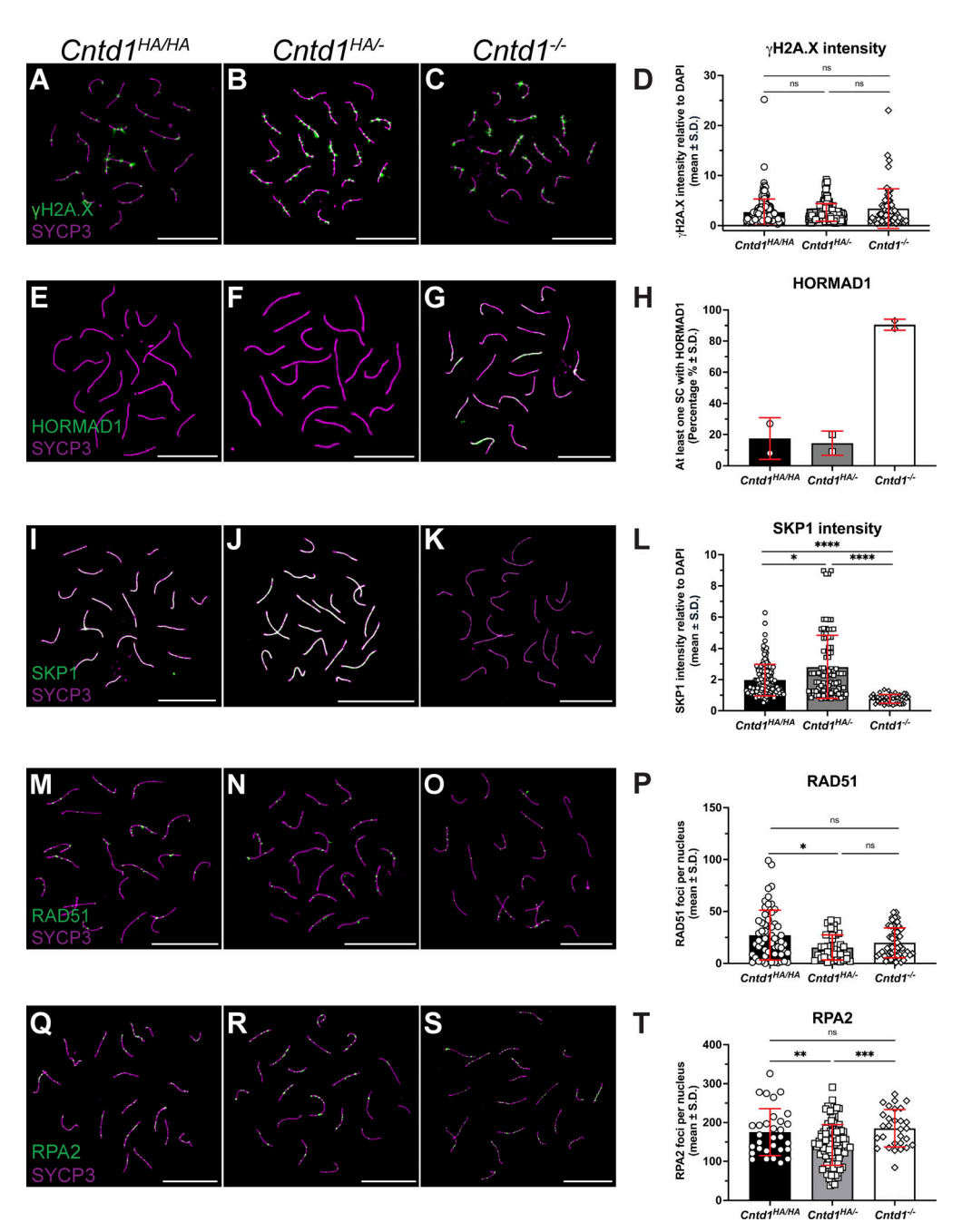


Figure S4. Early DSB repair in Cntd1-/- oocytes is normal. (A-S) Localization of (A-C) vH2A.X, (E-G) HORMAD1, (I-K) SKP1, (M-O) RAD51, and (Q-S) RPA2 (green) and SYCP3 (magenta) on chromosome spreads from Cntd1HA/HA, Cntd1HA/-, and Cntd1-/- oocytes at pachynema. (T) Quantification of (D) γH2A.X, (H), HORMAD1, (L) SKP1, (P) RAD51, and (T) RPA2. For yH2A.X: quantification of the intensity of yH2A.X normalized to DAPI in pachytene-staged cells (mean intensity in arbitrary units \pm SD) for $Cntd1^{HA/HA}$ (n=173 nuclei; 2.7 ± 2.6), $Cntd1^{HA/-}$ (n=151 nuclei; 2.7 ± 1.8), and $Cntd1^{-/-}$ (n=58 nuclei; 3.4 ± 4.0). Statistical analysis: $Cntd1^{HA/HA}$ and $Cntd1^{HA/-}$: P = 0.1868, $Cntd1^{HA/HA}$ and $Cntd1^{-/-}$: P = 0.7435, $Cntd1^{HA/-}$ and $Cntd1^{-/-}$: P = 0.7128. $n \ge 2$ pairs of ovaries were used. For the HORMAD1 analysis: (mean percentage \pm SD) Cntd1^{HA/HA} (HORMAD1 n=54 nuclei; 83 \pm 13), Cntd1^{HA/-} (HORMAD1 n=56 nuclei; 86 \pm 8.5), and Cntd1^{-/-} (HORMAD1 n = 55 nuclei; 9.5 ± 3.5). Statistical analysis: chi-square, P < 0.0001. $n \ge 2$ pairs of ovaries were used. For SKP1: quantification of the intensity of SKP1 normalized to DAPI in pachytene-staged cells (mean intensity in arbitrary units \pm SD) for $Cntd1^{HA/HA}$ (n = 140 nuclei; 2.0 ± 1.0), $Cntd1^{HA-}$ (n = 88 nuclei; 2.8 ± 2.0), and $Cntd1^{-/-}$ (n = 42 nuclei; 0.77 ± 0.28). Statistical analysis: $Cntd1^{HA/HA}$ and $Cntd1^{HA/-}$: P = 0.0197, $Cntd1^{HA/HA}$ and $Cntd1^{-/-}$: P < 0.0001, $Cntd1^{HA/-}$ and $Cntd1^{-/-}$: P < 0.0001, $Cntd1^{-/-}$: P < 0.0001, P < 0.0001, P < 0.0001, P < 0.0001, P $Cntd1^{-/-}$: P < 0.0001. $n \ge 2$ pairs of ovaries were used. For RAD51: (mean foci number \pm SD) $Cntd1^{HA/HA}$ (n = 58 nuclei; 27 \pm 24), $Cntd1^{HA/-}$ (n = 42 nuclei; 15 \pm 12), and Cntd1^{-/-} (n = 52 nuclei; 20 ± 14). Statistical analysis: Cntd1^{HA/HA} and Cntd1^{HA/-}: P = 0.029, Cntd1^{HA/HA} and Cntd1^{-/-}: P = 0.2385, Cntd1^{HA-} and Cntd1^{-/-}: P = 0.2385, Cntd1^{HA-} 0.1517. $n \ge 3$ pairs of ovaries were used. For RPA2: (mean foci number \pm SD) $Cntd1^{HA/HA}$ (n = 31 nuclei; 175 ± 60), $Cntd1^{HA/-}$ (n = 106 nuclei; 132 ± 152), and Cntd1^{-/-} (n = 29 nuclei; 167 ± 203). Statistical analysis: Cntd1^{HA/HA} and Cntd1^{HA/-}: P = 0.0032, Cntd1^{HA/HA} and Cntd1^{-/-}: P = 0.4949, Cntd1^{HA/-} and Cntd1^{-/-}: P = 0.4949, Cntd1^{HA/-} 0.0001. One pair of ovaries was used for $Cntd1^{HA/HA}$. For $Cntd1^{HA/-}$ and $Cntd1^{-/-}$, $n \ge 2$ pairs of ovaries were used. Pachynema-staged oocytes were determined using SYCP3 (absence of forks or bubbles). The mean and standard deviation lines are in red. White scale bars are equal to 20 µm. A Mann-Whitney test was used for yH2A.X, RAD51, and SKP1, and an unpaired t test was utilized for RPA2 to test statistical significance. P values are as follows: *P < 0.05, **P < 0.001, ***P < 0.0002, ****P < 0.0001.

Wood et al. Journal of Cell Biology

S4



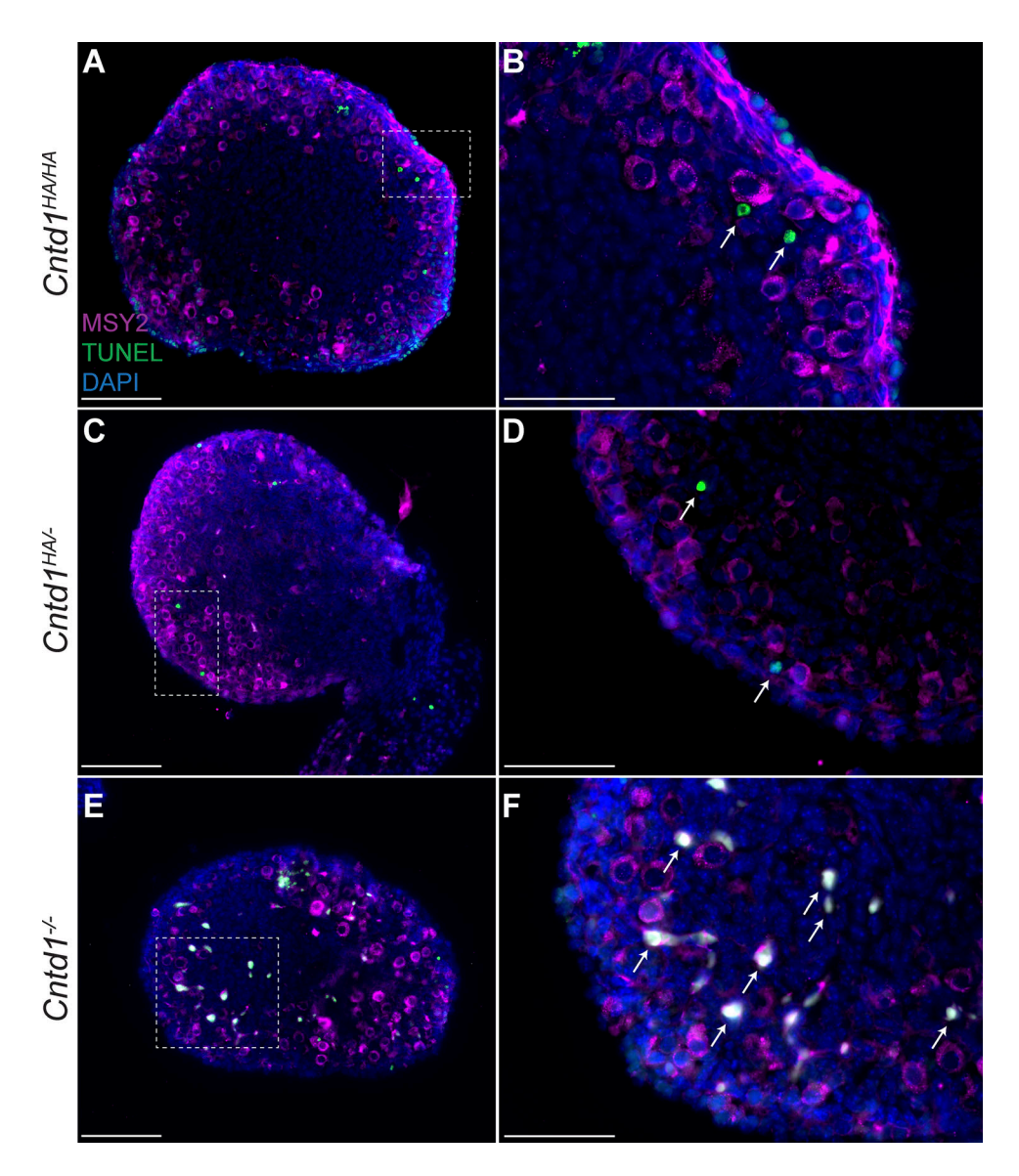


Figure S5. **Cntd1**^{-/-} **ovaries have an increase in TUNEL-positive cells. (A–F)** PND1 ovaries from (A) Cntd1^{HA/HA}, (C) Cntd1^{HA-}, and (E) Cntd1^{-/-} females stained with MSY2 (magenta), TUNEL (green), and DAPI (blue). Insets (white dashed square) for (B) Cntd1^{HA/HA}, (D) Cntd1^{HA/-}, and (F) Cntd1^{-/-} were captured at 40× magnification of TUNEL-positive cells (white arrows). Scale bars for A, C, and E are equal to 100 μm. Scale bars for B, D, and F are equal to 50 μm.

Provided online are Table S1, Table S2, and Table S3. Table S1 shows raw values, mean, and statistical results for Figs. 1, 4, 5, 6, and 7 in individual tabs. Table S2 shows raw oocyte and/or follicle counts and statistical results for Figs. 3, 8, and 9. Table S3 shows raw values, mean, and statistical results for Fig. S4.